Strength Enhancement of an Aluminum Alloy Through High Pressure Torsion

Uchechi Okeke[1,2], Hakan Yilmazer[3], Shigeo Sato[4], and Carl J. Boehlert[1]

[1]Department of Chemical Engineering and Materials Science, Michigan State University, East Lansing, U.S.A.; [2]Tank Automotive Research, Development, and Research Center, Warren, MI; [3]Department of Metallurgical and Materials Engineering, Yildiz Technical University, Istanbul, Turkey; [4]Toyohashi University of Technology, Toyohashi, Japan

Abstract

High-pressure torsion (HPT) was used to investigate the potential of grain refinement and strengthening achievable for aluminum alloy 2139-T8. Discs of 20mm diameter and approximately 0.9mm thickness were HPT processed at room temperature under an applied pressure of 5 GPa after 1, 2, 4 and 8 revolutions. Microstructural characterization of the HPT-processed discs showed the formation of a sub-micron grain structure after one revolution. The HPT processing led to an exceptional increase of the hardness and tensile strength after only one revolution as well as a relatively homogenous microstructure containing refined grains. Some grain growth occurred with increasing number of revolutions. X-ray diffraction line profile analysis suggested dislocation arrangements consistent with the microstructural evolution and strengthening behavior. Overall, this study confirmed that there is a potential for using HPT for manufacturing Al 2139 with enhanced hardness and tensile strength.

Keywords: high-pressure torsion; severe plastic deformation; ultrafine-grained;

Introduction

Material design introduces new challenges, especially when traditional materials are being replaced with other emerging material systems. For example, replacing steel with lightweight materials is an effective way to meet the demand for clean, efficient, and enhanced performance in the transportation industry [1]. Aluminum (Al) is a lightweight alternative that can achieve strengths that are comparable to some steel alloys when properly alloyed, heat treated, and worked [2]. Consequently, Al alloys, such as the 2xxx series (Cu-based Al alloys), are commonly used in the aerospace industry [3]. For the 2xxx series Al alloys, processing and heat treatment can enhance the microstructural and mechanical properties. In particular, Saccon et al. [4] found that an Al 2139 alloy, an age hardenable Al alloy which contains copper (Cu), magnesium (Mg), and silver (Ag), can exhibit attractive mechanical properties.

High pressure torsion (HPT), first proposed over 60 years ago, is a room-temperature (RT) severe plastic deformation (SPD) processing method that within the last 20 years has been increasingly investigated [5-28]. HPT refines the grains to submicron dimensions and this grain refinement improves strength and promotes superplasticity [29-31]. Grain refinement improves strength and superplasticity, and HPT has been performed on metals and alloys ranging from low tensile strength and high elongation-to-failure (ε_f) to high strength and low ε_f [6,7]. HPT of pure Al [8–10,23,24] and Al alloys [9–13,18,24-26] has been investigated primarily for strengthening purposes. HPT-processed materials generally show a significant enhancement of hardness and strength, as compared to their coarse-grained counterparts due to exceptional grain refinement as well as the introduction of crystal lattice defects [32]. GBs act as barriers that hinder dislocation motion, such that dislocation pile-ups develop at the GBs. As stated by the Hall-Petch relation, the yield strength of a material is inversely proportional to the square root of the grain size, and thus, the driving force for dislocations to penetrate the GBs is constrained in ultrafine grained materials.

It is clear in the literature that grain refinement of Al and its alloys can occur via solid state processes and SPD. HPT is such a process that refines the microstructure to submicron dimensions. The grain diameters of materials processed by HPT are reported as 160 nm (Al2024) [31], 300 nm (Al2024) at 673K [31], 130 nm 150 nm (Al-Mg-Sc) [29,30], 300 nm (Al-Cu-Zr) [33], 500 nm (A1050-pure Al) [34], 400 nm (A1100-pure Al) [35], 1.3 μm (4NAl) [35], 4.8 μm (5NAl) [35], 20 μm (6NAl) [35], 250 nm (Al-Mg-Si) [36], 120 nm (Al-Mg) [37], 620 nm (Al-Si-Sc) [38]. Such significant grain refinement leads to superplasticity for Al alloys [29-31,33].

The objective of the study was to explore how HPT effects the microstructure and the mechanical properties of Al 2139. In particular, one target of this work was to understand the microstructural evolution of Al 2139 as a function of the number of turns during HPT. Another objective was to examine the mechanical response of this alloy as a function of number of turns during HPT. Thus, this work was intended to shed light on understanding how HPT processing can further enhance the strengthening of precipitate-strengthened Al alloys and point to identifying attractive processing conditions (i.e. number of turns) for obtaining desired strengthening. Hardness and tensile tests were performed on the material before and after HPT processing. The microstructures were characterized using scanning electron microscopy (SEM), electron backscattered diffraction (EBSD), transmission electron microscopy (TEM), and X-ray diffraction (XRD) line profile analysis (XLPA).

Experimental

Materials and Sample Preparation

The rolled Al 2139-T8 material was received as a square plate of dimensions 300mm by

300mm by 25mm thick. This alloy underwent a T8 temper, used to form θ' and Ω precipitates in order to improve the tensile strength and crack resistance [39]. Samples of 20 mm diameter and 1 mm thickness were electrodischarge machined (EDM) through the thickness of the plate as depicted in Figure 1. The samples were then polished to a thickness of approximately 0.9 mm, see Figure 2(a). Samples underwent standard metallographic polishing procedures up to a 420 grit finish, which provided sufficient surface roughness to avoid slipping during the HPT processing. The samples were then annealed in a vacuum furnace at 460°C for one hour followed by water quenching. They were then stored in a vacuum chamber prior to HPT processing.

High Pressure Torsion (HPT) Processing

During HPT, a sample is placed between two anvils and subjected to a high hydrostatic pressure and simultaneous torsional straining through the rotation of one of the anvils. The shear strain, γ, introduced in the disc specimen during HPT processing is directly proportional to the number of rotations and the distance from the center of the disc. It is often expressed in terms of the equivalent Von Mises strain, ε_{eq}, which is given by the relationship [40]:

$$\varepsilon_{eq} = \frac{\gamma}{\sqrt{3}} = \frac{2\pi N r}{h\sqrt{3}} \tag{1}$$

where N is the number of revolutions, r is the radial distance measured from the disc center, and h is the disc height or thickness. It follows from Eq. (1) that the shear strain has a radial dependence, which leads to inevitable inhomogeneity both in the microstructure and in the hardness values across the disc radius. For example, in this work we would expect γ values ranging from ~30 for 1 turn to ~250 for 8 turns at half the radius of the disks. Nevertheless, both a high number of revolutions and a high applied pressures are effective in generating reasonably homogeneous microstructures and high hardness values [14,15]. HPT-processed materials generally show a significant enhancement of the mechanical properties, especially hardness and strength, as compared to their coarse-grained counterparts, due to exceptional grain refinement as well as a high concentration of crystal lattice defects [16]. Grain Boundaries (GBs) act as barriers that hinder dislocation motion, such that dislocation pile-ups develop at the GBs. As stated by the Hall-Petch relation, the yield strength of a material is inversely proportional to the square root of the grain size, and thus, the driving force for dislocations to penetrate the GBs is constrained in ultrafine grained (UFG) materials.

In this work, conventional HPT processing was conducted at RT with monotonic torsional straining using a quasi-constrained HPT facility. The HPT machine was comprised of one mobile anvil for rotation. The samples were placed in the depression on the lower anvil, see Figure 2(b), which was then raised to compress the specimens between the upper and lower anvils. Subsequent rotation of the lower anvil under pressure completed the HPT process. Both the top and bottom anvils were patterned to provide traction, see Figure 2(b), and grease was placed around the sample on the anvil to reduce friction. The revolutions used for separate discs were N=1, 2, 4, and 8 with a pressure of 5 GPa and a speed of 0.2 RPM. A representative HPT-processed sample is exhibited in Figure 2(c).

Tensile Testing and Vickers Hardness Characterization

For the HPT processed material, tensile samples were machined to a dogbone shape using EDM according to the dimensions stated in [17], where the gage section width, thickness, and length were 2 mm, 0.5 mm, and 3 mm, respectively. For the Al 2139 T8 processed material, a sample was EDM cut into a dogbone shape with a gage length of 35 mm, a gage section width of 7 mm, and a thickness of 1 mm. All samples were polished to remove the EDM surface layers. The RT tensile properties of the HPT-processed specimens were measured in air using a Shimadzu

AGS-20kN-G tensile machine (Kyoto, Japan) and SHiKiBU software (v3.22), where the displacement rate was 0.5mm/min. One sample was tested for each of the following number of revolutions; N=1, 2, 4, and 8. Due to the small size of these specimens, the strain was not measured but the displacement was recorded instead. For the Al 2139 T8 processed sample, the uniaxial tensile test was performed using a MTS® servo-hydraulic testing machine equipped with an MTS® Flex Test SE controller. The test was performed in an air environment at RT using a constant displacement rate of 0.025 mm/second, which corresponded to a strain rate of approximately $0.001s^{-1}$. Strain was measured using an alumina-arm extensometer, with a 12mm gauge length, spring-pressed to the side of the gage section.

Vickers hardness was performed using a Shimadzu HMV Microhardness Tester (Kyoto, Japan). The force used on the pre-HPT annealed sample was 100 grams and the force used on the HPT-processed samples was 1000 grams. The loading time was 15 seconds for all samples. Hardness values were measured on the HPT-processed samples' cross-sections from the center of the discs to the edges at 1mm increments.

Microscopy Characterization

Sample preparation for optical microscopy (OM), SEM, and EBSD analysis included polishing through 0.06 µm colloidal silica. Such samples were stored in a vacuum chamber until use. For OM, the samples were etched in Keller's solution prior to viewing. For the SEM and EBSD analysis, the samples were punched using a Gatan 3 mm diameter disc punch. Each resulting disc was then ion-milled at 4.5keV at an angle of 3 degrees for 30 minutes. Backscattered electron (BSE) and secondary electron (SE) images were acquired at the ½ radius locations using a JEOL JSM SEM at a beam voltage of 5kV. EBSD orientation maps were acquired using an EDAX (Mahwah, NJ) EBSD system. EDAX TSL OIM™ software (v6.2) was used to acquire and process the data. The EBSD orientation maps were acquired using a beam voltage of 25kV, a working distance of approximately 10mm, and a step size of 10nm. The average grain size for the N=8 processed samples was determined using the EBSD data. A minimum of 5° misorientation was used as the criteria for distinguishing separate grains. For the N=1, 2, and 4 processed samples, the average grains sizes were determined using TEM bright field (BF) photomicrographs, ImageJ software, and ASTM E112-13 [41]. For most of the conditions, over 150 grains were measured in this grain size analysis, while the minimum number of grains analyzed per condition was 82. The secondary phases' volume fractions were estimated using SEM photomicrographs and ImageJ software from the SEM images.

Bright field (BF) and dark field (DF) TEM photomicrographs and diffraction patterns were acquired using either a TOPCON EM-002B or a JEOL JEM-2000EXII TEM. The voltage used was 200kV. The TEM samples were mechanically polished to a thickness of approximately 150μm and then mechanically punched to a 3mm diameter disc. These samples were then electrochemically polished to perforation in an electrolyte solution containing 30% nitric acid and 70% methanol at -25°C and 12V. The samples were then ion milled at 4.5keV at an angle of inflection of 3° for 30 minutes.

X-ray Diffraction Line Profile Analysis (XLPA)

The X-ray diffraction measurements for the line profile analysis were performed in Bragg–Brentano (2θ–θ) geometry using an X-ray diffractometer equipped with a Cu Kα radiation source. X-rays were generated at 40 kV and 40 mA. The XLPA samples, with dimensions of 4 mm x 4 mm were taken at the half radius position of the HPT disk and polished through 2400 grit abrasive paper. Because X-ray scattering of white X-rays and the Cu $K\alpha_2$ component distorts the line profile, incident X-rays were monochromated to the Cu $K\alpha_1$ line (0.15406 nm) with a Johanssontype monochromator of quartz-101 reflection. The microstructure of the HPT samples was evaluated by X-ray Line Profile Analysis (XLPA) [42] using a Convolution Multiple Whole Profile (CMWP) fitting procedure [43] . The measured XRD profiles were fitted using a convolution profile, I,

$$I = I_s + I_m + I_i \tag{2}$$

where I_s is the function of the size of the smallest unit of a crystal aggregation, I_m is the function of microstrain, and I is the function of the instrumental effect. Ungar *et al.* [44] reported that the crystallite diameter, given by XLPA, provides the diameter of subgrain or dislocation cells bounded by small-angle grain boundaries or dipolar walls. The average diameter of the subgrains ($< x >_{area}$) was then calculated [43] by CMWP fitting as:

$$< x >_{area} = mexp(2.5\sigma^2) \tag{3}$$

where m is the median and σ is the size distribution function. The I_m used in the CMWP fitting was given by its Fourier transform, derived [45,46] as:

$$I_m = exp\left(-2\pi^2 g^2 L^2 < \varepsilon_{g,L}^2 >\right) \tag{4}$$

where g is the absolute value of the diffraction vector and L is the Fourier variable. $< \varepsilon_{g,L}^2 >$ is the mean square strain, defined [46] as:

$$\langle \varepsilon_{g,L}^2 \rangle = (\rho \bar{C} b^2 / 4\pi) f\left({}^{L}/_{R_e}\right) \tag{5}$$

where ρ, $\bar{C}$, b, R_e and f are the dislocation density, the contrast factor of dislocations, the absolute value of the Burgers vector, the Wilkens function, and the effective outer cut-off radius of dislocations, respectively [45–47]. The $f(L/R_e)$ function was determined for distributions of dislocations in the entire L range from zero to infinity [46]. However, confusion between the R_e and the coherence length and other length scales in crystallites has been reported [48]. In order to clearly demonstrate the dislocation arrangement during deformation, a suitable dimensionless parameter, M $\left(M = R_e\sqrt{\rho}\right)$, was introduced [49]. If the dislocations are a major source of microstrain in a cubic polycrystalline system, the contrast factors of dislocations, $\bar{C}$ can be averaged over the permutations of the *hkl* indices and defined [45] as:

$$\bar{C} = \bar{C}_{h00}(1 - qH^2) \tag{6}$$

where $\bar{C}_{h00}$ is a constant. H^2 is defined [44] as:

$$H^2 = (h^2k^2 + h^2l^2 + k^2l^2)/(h^2 + k^2 + l^2)^2 \tag{7}$$

Furthermore, the q parameter [48,50], which characterizes the anisotropic contrast effect of dislocations, depends on the elastic constants and the dislocation slip systems activated in the crystal. Finally, the instrumental profile (I_i) was prepared using the XRD profile of standard LaB_6 powders.

Results and Discussion

Microstructure

The OM photomicrograph in Figure 3 illustrates the microstructure of the Al 2139-T8 alloy after annealing at 460°C for one hour. For the Al-Cu-Mg-Ag alloys, the T8 temper brings out nanoscales plates (θ’, Ω) distributed homogeneously throughout the matrix grains [51,52]. The secondary phases coarsened slightly upon annealing, see Figure 4. The precipitate volume fraction before annealing was 0.01, while post annealing, the precipitate volume fraction was 0.08.

Grain refinement, to submicron dimensions, was evident in Figure 5, which provides BSE SEM photomicrographs of the HPT-processed microstructures at 5 mm from the center (½ radius) of the discs. The average grains dimensions are listed in Table I. At N=4 and N=8, grain growth was apparent, however, the grain size remained at the nanoscale. Ito et al. [10] reported that the grain growth happens at N>1/2 for pure Al by dislocation generation which includes the accumulation of dislocations, the formation of dislocation cells (subgrains with low angle boundaries), the enhancement of the misorientation and the annihilation of dislocations for ultrafine grains with high angle boundaries. In addition, the grain growth may be explained by the slight heating that may occur with increased number of revolutions (i.e. longer processing times) and greater strains achieved as these are associated with higher frictional heating, which may result in annealing and even recrystallization [19,20]. The secondary phase volume fractions were quite similar for all the HPT processed materials, see Table I. Figure 5 demonstrates that for N=1, 2, and 4, the precipitates were larger than the matrix grains. However, for N=8, the microstructure contained uniformly-distributed precipitates, which were smaller than the matrix grains. The larger of these precipitates were about the size of the matrix grains. Figures 6 and 7 illustrate EBSD inverse pole figures for the HPT samples at N=1 and N=8, respectively. The distribution of the precipitate phases (Al_2Cu, θ', and Al_2CuMg, S-type) was primarily intragranular for N=1 and intergranular for N=8.

The microstructure of the HPT samples was evaluated by XLPA using the CMWP fitting procedure, where Figure 8 shows the measured profile (open black circles) of a HPT sample, the fitted profile (red line), the difference between the measured and the fitted profiles (blue line), and the background baseline (green line). The parameters estimated by the CMWP fitting procedure from XRD profiles of HPT samples are summarized in Table II.

The XLPA also revealed that the HPT samples exhibited nanoscale subgrains in the range of 30-35 nm (see Table II) where the microstrain (non-uniform strain) was induced by numerous dislocations [43] and nanostructured secondary phases [53]. The significant increase in dislocation density (7.25×10^{14} m^{-2}) with shear strain (γ) in the range of $N \leq 1$, see Figure 9(a), is indicative of an accumulation of dislocations generated through the HPT processing due to entrapment by dislocations and precipitates. The high amount of dislocations was also suggested in the EBSD image indicating undistinguishable parts for the HPT sample at N=1 as shown in Figure 6. Thus, in order to minimize the internal strain energy [54], such large numbers of dislocations rearrange and annihilate (6.43 x 10^{14} m^{-2}) within grains to form dislocation cells and subgrains with the further γ increment in the range of $N \leq 2$, see Figure 9(a). Correspondingly, the subgrain diameter in the grains decreases in the range of $N \leq 4$, see Figure 9(b). The cell boundaries should evolve through annihilation of dislocations in order to form fine grains with boundaries upon the further γ increment [55,56]. At $N > 2$, however, the further γ increment suggested a balance between the formation and annihilation of dislocations at the cell/subgrain boundaries. At N > 4, the dislocation density decreased and the subgrain diameter saturated at approximately 31 nm; see Figure 9(a) and (b). A similar level of dislocation density saturation for Al 2139 (approximately 10^{14} m^{-2}) has also been reported for some metals subjected to SPD, such as Al [9], Al–Mg alloys [57,58], and Cu [59] (approximately 10^{14} m^{-2}). For example, grain refinement in pure Al is achieved at N=1, with subsequent recovery of dislocations and grain growth occurring when $N > 1$ [10]. Similar results have also been shown for pure Al [8,9,23,24]. In contrast to face-centered-cubic metals (i.e. Al), body-centered-cubic metals, such as Ti-Al-Nb-Zr (TNTZ) [6,17], exhibit a relatively slow microstructural refinement at $N \geq 10$. This can be explained by the high diffusion rate of vacancies in Al, as the diffusion of vacancies formed during deformation directly controls the annihilation of dislocations [60–62].

The XLPA also provides valuable information of the strain fields as they are related to the material's dislocation character. Figure 10(a) shows that the dislocation arrangement parameter (*M)* is less than 1. Relating to the intensity distribution, when the dislocations are properly arranged in HPT samples, the tail of the XRD profile approaches a Lorentzian function, and results in an M parameter of less than 1 [63,64]. Moreover, this M parameter decreases with decreasing dislocation density in the range of $N \geq 4$, see Figure 10(a), indicating a good relationship between these parameters with respect to the rearrangement and annihilation of dislocations and a homogeneous microstructural refinement.

The anisotropic contrast effect of dislocations on the peak broadening can be characterized by the q parameter in the averaged contrast factor, $\bar{C}$, of dislocations (see Equation 6) [48,50]. Fundamentally, this q parameter is related to the elastic constants and the dislocation slip systems activated in the crystal [48], and can be theoretically calculated for pure edge and screw dislocations [54] as:

$$q = a[1 - exp(A_i/b)] + cA_i + d \tag{8}$$

where $A_i = 2c_{44}/(c_{11} - c_{12}) = 1.22$, based on the elastic constants of $c_{11} = 1.06$, $c_{12} = 0.6$, and $c_{44} = 0.28$ reported for [65]. The microstructural parameters of the FCC system when $c_{12}/c_{14} = 2$ have been reported [48] as $a = 5.83$, $b = 0.81$, $c = 0.08$, and $d = -4.3$ for edge dislocations and $a = 5$, $b = 0.72$, $c = 0.07$, and $d = -3.19$ for screw dislocations. The upper limit of q is therefore determined as approximately 0.33 for pure edge dislocation and approximately 1.31 for pure screw dislocations in Al 2139. Since the average value of the lower and upper limits of the q (approximately 0.82 as gathered from Figure 9(b)) represents a random mixed-edge and screw-type dislocation characteristics, an estimated q by CMWP fitting that is close to the lower or upper limit suggests a high proportion of edge or screw dislocations, respectively.

The change in q with increasing γ in the range of $N \leq 2$ and decreasing γ in the range of $N > 2$ for HPT samples is shown Figure 10(b), along with the theoretical q parameters for pure edge and screw dislocations (blue and red lines, respectively). The estimated q value of approximately 0.96 at the start of deformation indicates that 64% screw and 36% edge dislocations are present;

however, this q value drastically increased to ~1.08 (76% screw, 24% edge) at N=2 and gradually decreased to approximately 0.82 at N=8. Since this value is equal to the average, it means that with increasing γ, the mixed character of the dislocations becomes stronger in the prevailing slip system of $a/2<110>\{111\}$, where a is the lattice constant. In other words, the screw dislocations have been annihilated by climb with increasing γ [61].

The decreasing tendency of the M and q parameters with dislocation density indicates the annihilation of dislocations is dominant when $N \geq 4$ [66], and is supported by clear boundaries and subgrains evident in the microstructure of a HPT processed TNTZ alloy [6,17] and also in the BF TEM images in Figure 11 of the current study. Considering the high dislocation density, such boundaries are indicative of extra dislocations that do not play a part in the formation of misorientations and vacancies at the boundaries [67], but nevertheless lead to a relatively high internal strain energy. These so-called non-equilibrium boundaries [68,69] have been reported in several SPD experiments [70,71]; the low misorientation between neighboring grains and subgrains is evident from the incomplete Debye rings in the SAED patterns (see Figure 11(a)), indicating that they exhibit low-angle characteristics when $N < 2$. In contrast, the complete Debye rings in the SAED patterns at $N \geq 2$, see Figure 11(b), (c), and (d), confirm that these low-angle boundaries are transformed into high-angle boundaries with an increase in γ [53,71,72]. Similar observations have been recorded for a HPT-processed TNTZ alloy [6,17].

A BF TEM image and along with the associated SAED patterns of the Al 2139-T8 microstructure is shown in Figure 12. The microstructure consisted of the θ' and Ω precipitates surrounded by the Al alloy matrix. These precipitates were homogeneously distributed in the matrix and exhibited a plate-like morphology with their lengths typically ranging from 50-120 nm. Representative TEM BF images of the HPT samples are shown in Figure 11 along with the associated SAED patterns. Unlike that for the Al 2139-T8 samples, the secondary phases were difficult to distinguish in the matrix of the HPT samples. The BF image at N =1 revealed wavy grain boundaries. Due to the expected high dislocation density, such boundaries are suggestive of exterior dislocations that may not play a significant role in the formation of vacancies at the boundaries [67], but nevertheless lead to a relatively high internal strain energy. Therefore, they are called non-equilibrium boundaries [68,69] and have been reported in several SPD studies [69,70]. The low misorientation between the neighboring grains and subgrains was also evident from the incomplete Debye ring at N=1, indicating low-angle misorientation characteristics of such grains. The TEM BF image of $N \geq 2$ (see Figure 11) shows that the grains exhibited average diameters less than one hundred nanometers (see Table I). Furthermore, the grains contain nanostructured subgrains. In addition, the grains were surrounded by clearly-distinguished boundaries. The SAED patterns at $N \geq 2$ show more complete Debye rings. The complete Debye rings in the SAED patterns at $N \geq 2$ confirm that the low-angle boundaries were transformed into high-angle boundaries, which is expected with an increment in γ [54,71,73].

Mechanical Behavior

The average hardness of the Al 2139-T8 was measured to be 178 Hv, see Figure 13. After annealing, the hardness value dropped to 80Hv. The hardness profile of the HPT processed samples as a function of revolution is shown in Figure 13. These values were always at least two times higher than that of the annealed material and in some cases they reached as high as three times the annealed material. In the center of the discs, the hardness values varied among the revolutions. For N=1, the hardness seemed to slowly increase throughout the entire radius of the disc, which suggests a heterogeneous microstructure at a lower strain level, which has been observed for pure Al at N≤1 [10]. The increasing hardness through radius and high dislocation density highest at N=1, suggests that the microstructure contained a high fraction of low angle boundaries and interfaces, indicating dislocations and the fragmentation of grain boundaries occurred similar to that reported in [10]. However, for N≥1, the hardness values 1 mm from the center through the edge of the sample (full radius) were approximately the same, with the exception being for N=8, where the hardness appeared to be a maximum at 5mm from the center of the disc (i.e. ½ radius) and then decreased slightly with increased distance from the center of the disc. Grain size coarsening also happens in pure Al at N>1/2 and this results in a similar hardness decline [10]. This is contrary to what happens for hybrids, where the hardness increase from the center to the sample edge is explained partially by intermetallic formation [20,21,74]. Thus, it appears that the grain size coarsening experienced for the N=8 material resulted in decreased hardness values. It is evident that one revolution is necessary to achieve an ultrafine-grained material having high hardness that exhibits relatively uniform hardness at a distance of greater than or equal to 2mm from the center of the discs. The relatively homogenous ultrafine-grained microstructure, with the precipitates dispersed uniformly within the matrix grains, for the N=1 sample as compared with the N≥2 samples, see Figures 5-7, can help explain this result. The hardness values at the center of the disk were 174, 250, 223, and 198 for N=1, 2, 4, and 8, respectively, see Table III. The hardness value at the center for N=1 is negligibly lower than the annealed condition. With further rotations, the hardness increases (N=2) then decreases (N ≥ 4). At the full radius of the disk, hardness values were 238, 245, 239, and 214 for N=1, 2, 4, and 8, respectively. This trend is expected to be related to the corresponding dislocation density and subgrain diameter trend exhibited in Figure 9. At ½ radius, which is where the CMWP analysis was performed, the trend in HV was N=1 < N=2 < N=4, 8. This is an inverse relationship to the subgrain diameter (Fig. 9b) in which the highest HV had the lowest subgrain diameters. Increasing rotations reduced the subgrain diameter size and which increased the hardness.

The above results are in agreement with the tensile property results. Figure 14(a) illustrates the engineering stress versus strain for the T8 sample. Figure 14(b) illustrates the engineering stress versus displacement curves for the HPT processed samples as a function of the number of revolutions. The trend of the decreasing tensile strength with increasing number of revolutions is also in agreement with the dislocation density (see Figure 9a). For the N=1, 2 and 4, the ultimate tensile strengths were about twice that for the T8 sample, where the N=8 sample exhibited less of an increase in strength. Thus, it appears that the grain coarsening experienced by the N=8 sample resulted in a decrease in strengthening as would be expected from the Hall-Petch relationship [75, 76]. These results are also consistent with the XLPA results, where a change in the dislocation arrangements occurred with increased number of revolutions. Furthermore, the TEM observations of the N>1 HPT samples are consistent with the idea that the microstructure underwent recovery with dislocations annihilation followed by grain coarsening with dislocation rearrangement for increasing N, similar to other studies [59,77,78]. Therefore, the decrease in strengthening can be explained by the increasing grain diameter and the rearrangement and absorption of dislocations during recovery and growth. In addition, any inhomogeneities in the microstructures across the radial sections would be expected to result in a variation of the mechanical properties and strengthening. One revolution was enough to increase the strength significantly while maintaining ductility. N=1 exhibited the highest dislocation density and subgrain diameter. With subsequent revolutions, the alloy did not exhibit greater tensile strengths and the ε_f values decreased. At N=2 and N=8, dislocation annihilation was evident as tensile strengths and dislocation density decreased significantly. Overall, this work established that for Al 2139, one revolution of HPT processing can result in a refined microstructure with exceptional strengthening without a deleterious debit in ε_f.

Summary and Conclusions

HPT processing was used to investigate the grain refinement and strengthening potential of Al alloy 2139-T8. Alloy discs were processed at RT under an applied pressure of 5 GPa through 1, 2, 4, and 8 revolutions. The HPT processing led to submicron grain refinement and an associated increase of the hardness and tensile strength after only one revolution. After 8 revolutions a greater variation in the microstructure occurred where some grain growth was observed, which helped explain the decrease in hardness and tensile strengths observed. XLPA suggested dislocation arrangements and evolution consistent with both the microstructural evolution observed by TEM and the strengthening behavior. Overall, HPT processing of Al 2139-T8 shows promise for producing lightweight materials with exceptional strengths.

Acknowledgments

This work was supported by the National Science Foundation Division of Material Research (Grant Nos. DMR1107117 and DMR1607942). The electron microscopy was performed under the National Science Foundation East Asia and Pacific Summer Institute Fellowship (Award No. 1515111) at the Institute of Materials Research (IMR) Tohoku University in Sendai, Japan. Acknowledgement is provided to Drs Mitsuo Niinomi and Huihong Liu for their technical support. Acknowledgement also goes to Dr. Makoto Nagasako and Shun Ito at the IMR Tohoku University for help with acquiring the TEM images. The HPT processing was carried out at Toyohashi University of Technology in Toyohashi, Japan under the supervision of Professor Yoshikazu Todaka). The Al 2139 Al alloy plate material was supplied by Dr. Tomoko Sano of the U.S. Army Research Laboratory.

The raw/processed data required to reproduce these findings cannot be shared at this time as the data also forms part of an ongoing study.

1 References

[1] L. Cheah, J. Heywood, Meeting U.S. passenger vehicle fuel economy standards in 2016 and beyond, Energy Policy. 39 (2011) 454–466.

[2] R. Schneider, B. Heine, R.J. Grant, Mechanical Behaviour of Commercial Aluminium Wrought Alloys at Low Temperatures, in: W.A. Monteiro (Ed.), Light Met. Alloys Appl., InTech, 2014.

[3] J.C. Williams, E.A. Starke Jr., Progress in structural materials for aerospace systems, Acta Mater. 51 (2003) 5775–5799.

[4] V.T. Saccon, B.S. Parra, C.W. Olea, J.F. dos Santos, N.G. de Alcântara, Microstructural characterization and mechanical behavior of an AA2139 T3 and T8 aluminum alloy joined by friction stir welding (FSW), Soldag. Amp Insp. 15 (2010) 289–297.

[5] A.P. Zhilyaev, T.G. Langdon, Using high-pressure torsion for metal processing: Fundamentals and applications, Prog. Mater. Sci. 53 (2008) 893–979.

[6] H. Yilmazer, M. Niinomi, K. Cho, M. Nakai, J. Hieda, S. Sato, Y. Todaka, Microstructural evolution of precipitation-hardened β-type titanium alloy through high-pressure torsion, Acta Mater. 80 (2014) 172–182.

[7] Y. Chen, N. Gao, G. Sha, S.P. Ringer, M.J. Starink, Strengthening of an Al–Cu–Mg alloy processed by high-pressure torsion due to clusters, defects and defect–cluster complexes, Mater. Sci. Eng. A. 627 (2015) 10–20.

[8] D. Orlov, Y. Todaka, M. Umemoto, N. Tsuji, Formation of bimodal grain structures in high purity Al by reversal high pressure torsion, Scr. Mater. 64 (2011) 498–501.

[9] A.P. Zhilyaev, K. Oh-ishi, T.G. Langdon, T.R. McNelley, Microstructural evolution in commercial purity aluminum during high-pressure torsion, Mater. Sci. Eng. A. 410–411 (2005) 277–280.

[10] Y. Ito, Z. Horita, Microstructural evolution in pure aluminum processed by high-pressure torsion, Mater. Sci. Eng. A. 503 (2009) 32–36.

[11] I.F. Mohamed, Y. Yonenaga, S. Lee, K. Edalati, Z. Horita, Age hardening and thermal stability of Al–Cu alloy processed by high-pressure torsion, Mater. Sci. Eng. A. 627 (2015) 111–118.

[12] I.F. Mohamed, S. Lee, K. Edalati, Z. Horita, S. Hirosawa, K. Matsuda, D. Terada, Aging Behavior of Al 6061 Alloy Processed by High-Pressure Torsion and Subsequent Aging, Metall. Mater. Trans. A. 46 (2015) 2664–2673.

[13] R. Vafaei, M.R. Toroghinejad, R. Pippan, Evaluation of mechanical behavior of nano-grained 2024 Al alloy during high pressure torsion (HPT) process at various temperatures, Mater. Sci. Eng. A. 536 (2012) 73–81.

[14] H. Jiang, Y.T. Zhu, D.P. Butt, I. V. Alexandrov, T.C. Lowe, Microstructural evolution, microhardness and thermal stability of HPT-processed Cu, Mater. Sci. Eng. A. 290 (2000) 128–138.

[15] A.P. Zhilyaev, S. Lee, G. V Nurislamova, R.Z. Valiev, T.G. Langdon, Microhardness and Microstructural Evolution in Pure Nickel During High-Pressure Torsion, 44 (2001) 2753–2758.

[16] T.G. Langdon, Twenty-five years of ultrafine-grained materials: Achieving exceptional properties through grain refinement, Acta Mater. 61 (2013) 7035–7059.

[17] H. Yilmazer, M. Niinomi, M. Nakai, K. Cho, J. Hieda, Y. Todaka, T. Miyazaki, Mechanical properties of a medical β-type titanium alloy with specific microstructural evolution through high-pressure torsion, Mater. Sci. Eng. C. 33 (2013) 2499–2507.

[18] K. Oh-ishi, K. Edalati, H.S. Kim, K. Hono, Z. Horita, High-pressure torsion for enhanced atomic diffusion and promoting solid-state reactions in the aluminum–copper system, Acta Mater. 61 (2013) 3482–3489.

[19] M. Kawasaki, B. Ahn, H. Lee, A.P. Zhilyaev, T.G. Langdon, Using high-pressure torsion to process an aluminum–magnesium nanocomposite through diffusion bonding, J. Mater. Res. 31 (2016) 88–99.

[20] M. Kawasaki, J.-K. Han, D.-H. Lee, J. Jang, T.G. Langdon, Fabrication of nanocomposites through diffusion bonding under high-pressure torsion, J. Mater. Res. (2018) 1–11.

[21] B. Ahn, H.-J. Lee, I.-C. Choi, M. Kawasaki, J.-I. Jang, T.G. Langdon, Micro-Mechanical Behavior of an Exceptionally Strong Metal Matrix Nanocomposite Processed by High-Pressure Torsion, Adv. Eng. Mater. 18 (2016) 1001–1008.

[22] J.K. Han, H.J. Lee, J. il Jang, M. Kawasaki, T.G. Langdon, Micro-mechanical and tribological properties of aluminum-magnesium nanocomposites processed by high-pressure torsion, Mater. Sci. Eng. A. 684 (2017) 318–327.

[23] N.Q. Chinh, P. Szommera, T. Csanadi, T.G. Langdon, Flow processes at low temperatures in ultrafine-grained aluminum., Mater. Sci. Eng. *A* **2006**, *434*, 326-334.

[24] M. Kawasaki, S.N. Alhajeri, C. Xu, T.G. Langdon, The development of hardness homogeneity in pure aluminum and aluminum alloy disks processed by high-pressure torsion Mater. Sci. Eng. A **2011**, *529*, 345-351.

[25] S. Panda, L.S. Toth, J-J Fundenberger, O. Perroud, J. Guyon, J. Zou, T. Grosdidier, Analysis of heterogeneities in strain and microstructure in aluminum alloy and magnesium processed by high-pressure torsion, Materials Characterization 2017, 123, 159-165,

[26] K. Edalati, Z. Horita, Significance of homologous temperature in softening behavior and grain size of pure metals processed by high-pressure torsion, Mater. Sci. Eng. A **2011**, *528*, 7514-7523. Issue 25-26,

[27] K. Edalati, Z. Horita, A review on high-pressure torsion (HPT) from 1935 to 1988, Mater. Sci. Eng. A 2016, 652, 325-352.

[28] K. Edalati, R. Miresmaeili, Z. Horita, H. Kanayama, R. Pippan, Significance of temperature increase in processing by high-pressure torsion, Mater. Sci. Eng. A. 528 (2011) 7301–7305.

[29] G. Sakai, Z. Horita, T.G. Langdon, Grain refinement and superplasticity in an aluminum alloy processed by high-pressure torsion, Mater. Sci. and Eng. A 393 (2005) 344–351.

[30] Z. Horita, T.G. Langdon, Achieving exceptional superplasticity in a bulk aluminum alloy processed by high-pressure torsion, Scripta Materialia 58 (2008) 1029–1032.

[31] S.V. Dobatkin, E.N. Bastarache, G. Sakai, T. Fujita, Z. Horita, T.G. Langdon, Grain refinement and superplastic flow in an aluminum alloy processed by high-pressure torsion, Mater. Sci. and Eng. A 408 (2005) 141–146.

[32] T.G. Langdon, Twenty-five years of ultrafine-grained materials: Achieving exceptional properties through grain refinement, Acta Mater. 61 (2013) 7035–7059.

[33] R.Z. Valiev, O.A. Kaibyshev, R.I. Kuznetsov, R.S. Musalimov, N.K. Tsenev, Low-temperature superplasticity of metallic materials, Dokl. Akad. Nauk. SSSR 301 (1988) 864–866.

[34] Y. Todaka, M. Umemoto, A. Yamazaki, J. Sasaki, K. Tsuchiya, Influence of High-Pressure

Torsion Straining Conditions on Microstructure Evolution in Commercial Purity Aluminum, Materials Transactions, 49(1) (2008) 7–14.

[35] Y. Ito, K. Edalati, Z. Horita, High-pressure torsion of aluminum with ultrahigh purity (99.9999%) and occurrence of inverse Hall-Petch relationship, Mater. Sci. and Eng. A 679 (2017) 428–434.

[36] A. Loucif, R.B. Figueiredo, M. Kawasaki, T. Baudin, F. Brisset, R. Chemam, T.G. Langdon, Effect of aging on microstructural development in an Al–Mg–Si alloy processed by high-pressure torsion, J Mater Sci 47 (2012) 7815–7820.

[37] M. Liu, H.J. Roven, M. Murashkin, R.Z. Valiev, Structural characterization by high-resolution electron microscopy of an Al–Mg alloy processed by high-pressure torsion,Mater Sci and Eng A 503 (2009) 122–125.

[38] V. Rajinikanth, K. Venkateswarlu, M.K. Sen, M. Das, S.N. Alhajeri, T.G. Langdon, Influence of scandium on an Al–2% Si alloy processed by high-pressure torsion, Mater. Sci. and Eng. A 528 (2011) 1702–1706.

[39] A. Cho, B. Bes, Damage Tolerance Capability of an Al-Cu-Mg-Ag Alloy (2139), Mater. Sci. Forum. 519–521 (2006) 603–608.

[40] R.Z. Valiev, Y.V. Ivanisenko, E.F. Rauch, B. Baudelet, Structure and deformaton behaviour of Armco iron subjected to severe plastic deformation, Acta Mater. 44 (1996) 4705–4712.

[41] Standard Test Methods for Determining Average Grain Size, ASTM International, West Conshohocken, PA, 2013.

[42] L. Li, T. Ungár, Y.D. Wang, G.J. Fan, Y.L. Yang, N. Jia, Y. Ren, G. Tichy, J. Lendvai, H. Choo, P.K. Liaw, Simultaneous reductions of dislocation and twin densities with grain growth during cold rolling in a nanocrystalline Ni–Fe alloy, Scr. Mater. 60 (2009) 317–320.

[43] T. Ungár, J. Gubicza, G. Ribárik, A. Borbély, Crystallite size distribution and dislocation structure determined by diffraction profile analysis: principles and practical application to cubic and hexagonal crystals, J. Appl. Crystallogr. 34 (2001) 298–310.

[44] T. Ungár, G. Tichy, J. Gubicza, R.J. Hellmig, Correlation between subgrains and coherently scattering domains, Powder Diffr. 20 (2005) 366–375.

[45] T. Ungár, G. Tichy, The Effect of Dislocation Contrast on X-Ray Line Profiles in Untextured Polycrystals, Phys. Status Solidi A. 171 (1999) 425–434.

[46] M. Wilkens, Theoretical aspects of kinematical X-ray diffraction profiles from crystals containing dislocation distributions(Fourier transform of X ray diffraction line profiles from crystals with dislocations), NBS Fundam. Asp. Dislocation Theory. 2 (1970).

[47] G. Ribárik, T. Ungár, J. Gubicza, MWP-fit: a program for multiple whole-profile fitting of diffraction peak profiles by ab initio theoretical functions, J. Appl. Crystallogr. 34 (2001) 669–676.

[48] T. Ungár, I. Dragomir, Á.;. Révész, A. Borbély, The contrast factors of dislocations in cubic crystals the dislocation model of strain anisotropy in practice, J. Appl. Crystallogr. 32 (1999) 992–1002.

[49] M. Wilkens, M. Wilkens, Acta Metall. 17, 1155 (1969). Acta Met. 17 (1969) 1155.

[50] I.C. Dragomir, T. Ungár, Contrast factors of dislocations in the hexagonal crystal system, J. Appl. Crystallogr. 35 (2002) 556–564.

[51] I. J. Polmear, The Effects of Small Additions of Silver on the Aging of Some Aluminum Alloys, Trans. Meallurgical Soc. O AIME. 230 (1964) 1331–1339.

[52] Q. Li, R.N. Shenoy, DSC and TEM characterizations of thermal stability of an Al–Cu–Mg–Ag alloy, J. Mater. Sci. 32 (1997) 3401–3406.

[53] T. Ungár, Microstructural parameters from X-ray diffraction peak broadening, Scr. Mater. 51 (2004) 777–781.

[54] D.A. Hughes, Microstructural evolution in a non-cell forming metal: Al□Mg, Acta Metall. Mater. 41 (1993) 1421–1430.

[55] Q. Wei, H. Zhang, B. Schuster, K. Ramesh, R.Z. Valiev, L. Kesckes, R. Dowding, L. Magness, K. Cho, Microstructure and mechanical properties of super-strong nanocrystalline tungsten processed by high-pressure torsion, Acta Mater. 54 (2006) 4079–4089.

[56] D. Kuhlmann-Wilsdorf, N. Hansen, Geometrically necessary, incidental and subgrain boundaries, Scr. Metall. Mater. 25 (1991) 1557–1562.

[57] J. Gubicza, N.Q. Chinh, Z. Horita, T.G. Langdon, Effect of Mg addition on microstructure and mechanical properties of aluminum, Mater. Sci. Eng. A. 387–389 (2004) 55–59.

[58] K. Oh-ishi, Z. Horita, D.J. Smith, T.G. Langdon, Grain boundary structure in Al–Mg and Al–Mg–Sc alloys after equal-channel angular pressing, J. Mater. Res. 16 (2011) 583–589.

[59] J. Gubicza, N.H. Nam, L. Balogh, R.J. Hellmig, V. V Stolyarov, Y. Estrin, T. Ungár, Microstructure of severely deformed metals determined by X-ray peak profile analysis, J. Alloys Compd. 378 (2004) 248–252.

[60] F.D. Fischer, J. Svoboda, F. Appel, E. Kozeschnik, Modeling of excess vacancy annihilation at different types of sinks, Acta Mater. 59 (2011) 3463–3472.

[61] B.J. Bonarski, E. Schafler, B. Mingler, W. Skrotzki, B. Mikulowski, M.J. Zehetbauer, Texture evolution of Mg during high-pressure torsion, J. Mater. Sci. 43 (2008) 7513–7518.

[62] E. Schafler, Strength response upon pressure release after high pressure torsion deformation, Scr. Mater. 64 (2011) 130–132.

[63] I. Groma, X-ray line broadening due to an inhomogeneous dislocation distribution, Phys. Rev. B. 57 (1998) 7535–7542.

[64] M. Wilkens, Quantitative interpretation of X-ray line broadening of plastically deformed crystals, J. Appl. Crystallogr. 8 (1975) 191–192.

[65] G. Simmons, H. Wang, Single crystal elastic constants and calculated aggregate properties: a handbook, 2d ed, M.I.T. Press, Cambridge, Mass, 1971.

[66] T. Ungár, E. Schafler, J. Gubicza, Microstructure of bulk nanomaterials determined by X-ray line profile analysis, in: M. Zehetbauer, Y. Zhu (Eds.), Bulk Nanostructured Mater., Wiley-VCH, Weinheim, 2009: pp. 361–386.

[67] X.G. Qiao, N. Gao, M.J. Starink, A model of grain refinement and strengthening of Al alloys due to cold severe plastic deformation, Philos. Mag. 92 (2012) 446–470.

[68] Ruslan Valiev, Nanostructuring of metals by severe plastic deformation for advanced properties, Nature. (2004) 511–516.

[69] A.A. Nazarov, A.E. Romanov, R.Z. Valiev, On the structure, stress fields and energy of nonequilibrium grain boundaries, Acta Metall. Mater. 41 (1993) 1033–1040.

[70] S. V. Divinski, G. Reglitz, H. Rösner, Y. Estrin, G. Wilde, Ultra-fast diffusion channels in pure Ni severely deformed by equal-channel angular pressing, Acta Mater. 59 (2011) 1974–1985.

[71] R.Z. Valiev, I. V Alexandrov, Y.T. Zhu, T.C. Lowe, Paradox of Strength and Ductility in Metals Processed by Severe Plastic Deformation, J Mater Res. 17 (2002) 5–8.

[72] F. Dalla Torre, R. Lapovok, J. Sandlin, P.F. Thomson, C.H.J. Davies, E.V. Pereloma, Microstructures and properties of copper processed by equal channel angular extrusion for

1–16 passes, Acta Mater. 52 (2004) 4819–4832.

[73] D. Hughes, N. Hansen, Microstructure and strength of nickel at large strains, Acta Mater. 48 (2000) 2985–3004.

[74] D. Escobar, Z.U. Raman, H. Yilmazer, M. Kawasaki, and C.J. Boehlert, Microstructural evolution and intermetallic formation in Zn-Mg hybrids processed by High-Pressure Torsion, Philosophical Magazine, Vol. 99 Issue 5 (2019) pp. 557-584.

[75] R.Z. Valiev, E.V. Kozlov, Yu.F. Ivanov, J. Lian, A.A. Nazarov, B. Baudelet, Acta Metall. Mater. 42 (1994) 2467–2475.

[76] S. Gourdet, F. Montheillet, Acta Mater. 51 (2003) 2685–2699.

[77] V.V. Stolyarov, Y.T. Zhu, T.C. Lowe, R.K. Islamgaliev, R.Z. Valiev, Nanostruct. Mater. 11 (1999) 947–954.

[78] I.P. Semenova, G.Kh. Salimgareeva, V.V. Latysh, T. Lowe, R.Z. Valiev, Mater. Sci. Eng., A 503 (2009) 92–95.

2

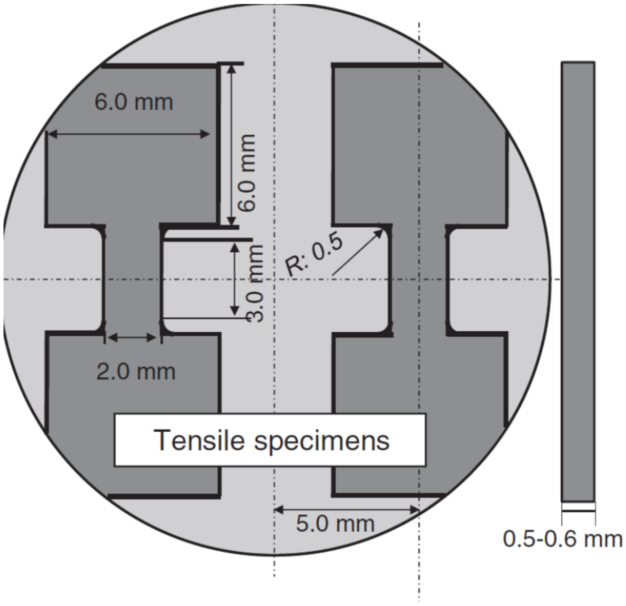

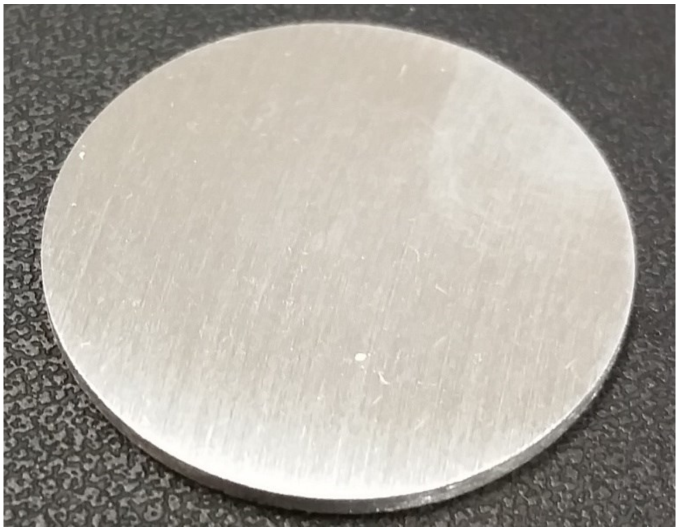

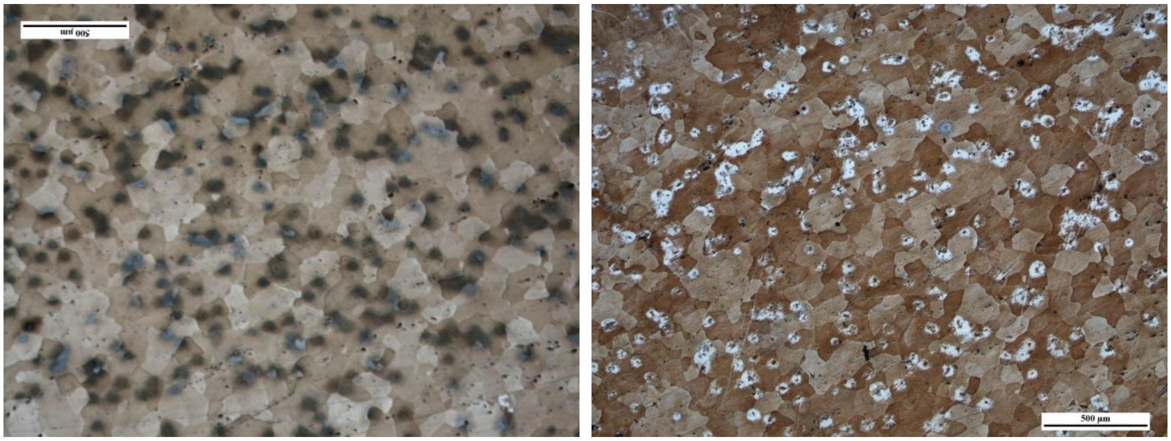

Before and after annealing at 460C for 1hr with etching

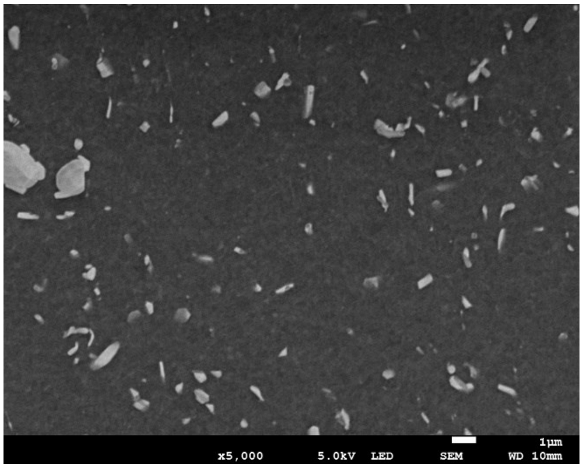

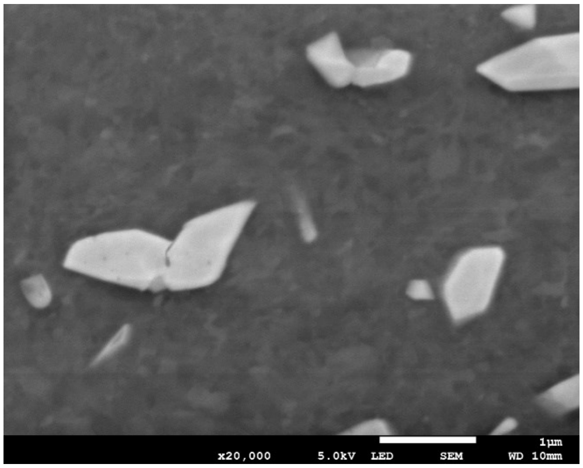

N=1, 5KX, 20K, 5 mm from the center (1/2 radius)

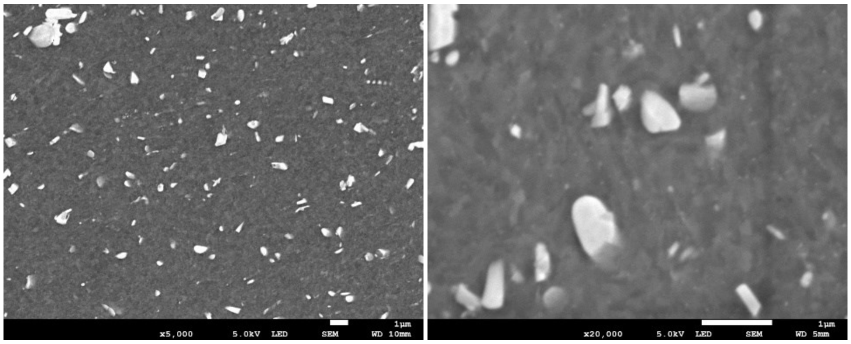

N=2,

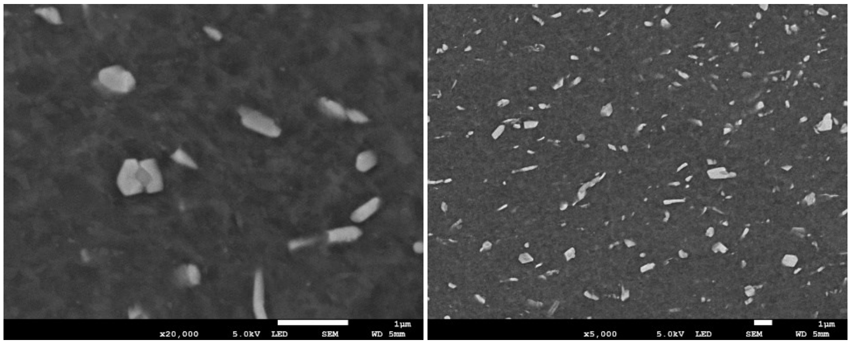

N=4

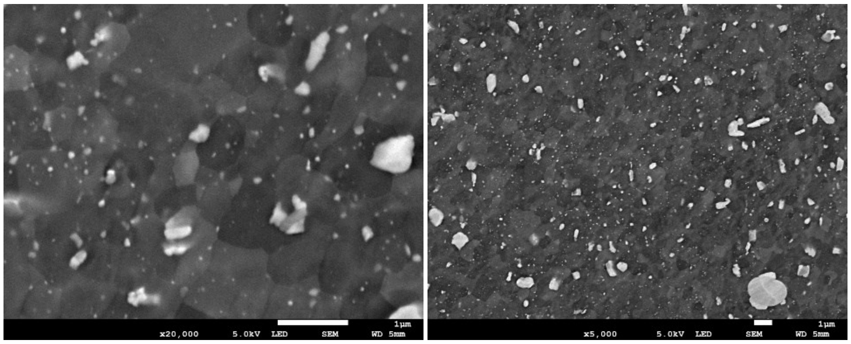

N=8

N=1, 5MM FROM CENTER

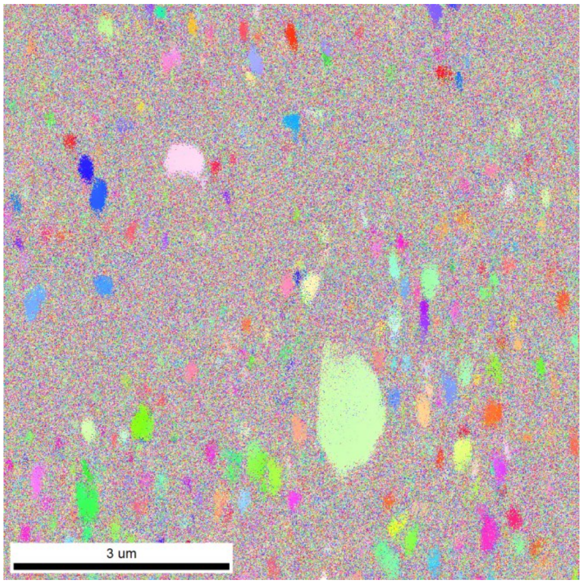

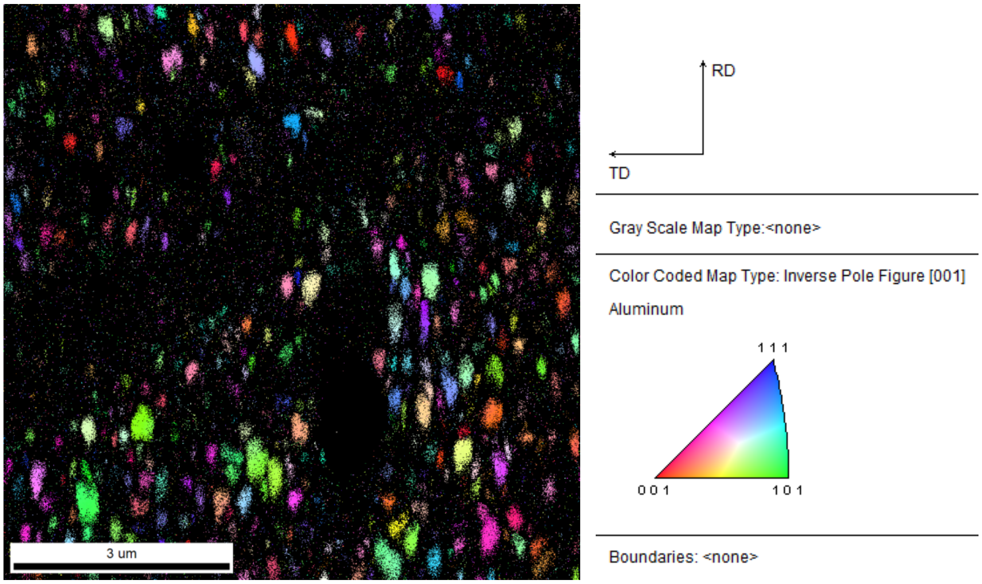
3 um
RD
TD
Gray Scale Map Type:<none>
Color Coded Map Type: Inverse Pole Figure [001]
Aluminum
1 1 1
0 0 1
1 0 1
Boundaries: <none>

Al

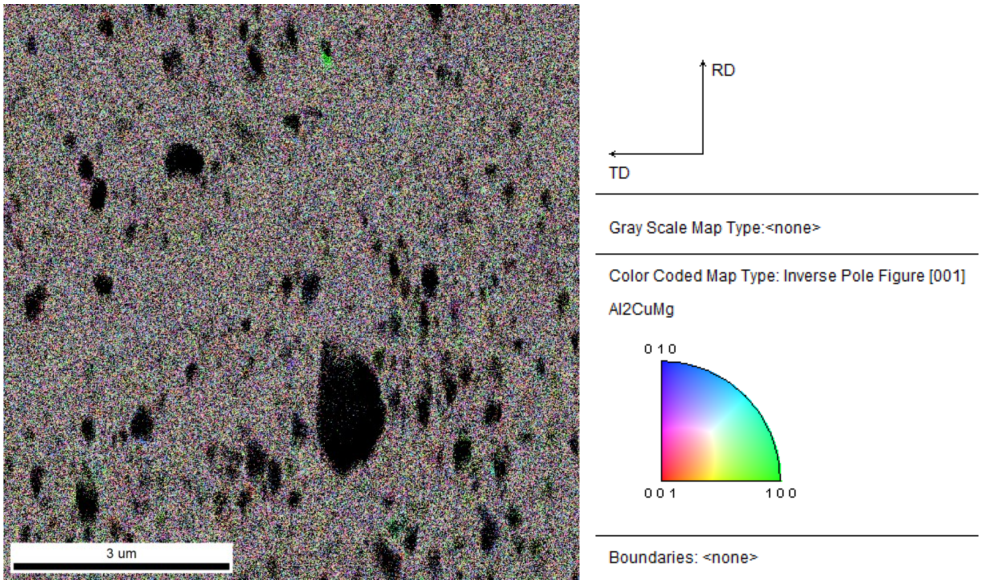
3 um
RD
TD
Gray Scale Map Type:<none>
Color Coded Map Type: Inverse Pole Figure [001]
Al2CuMg
0 1 0
0 0 1
1 0 0
Boundaries: <none>

al2cumg

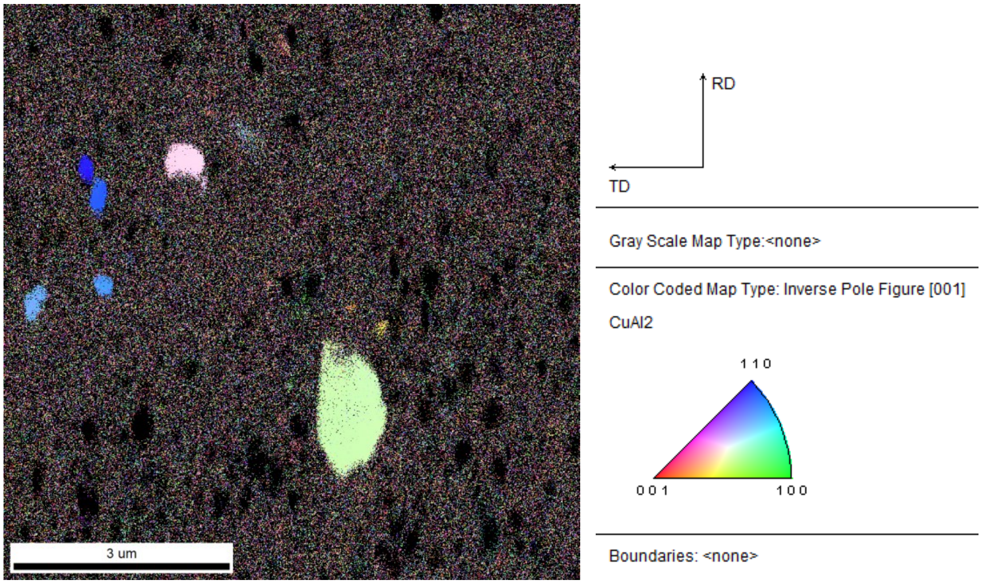

al2cu

N=8, 5MM FROM CENTER

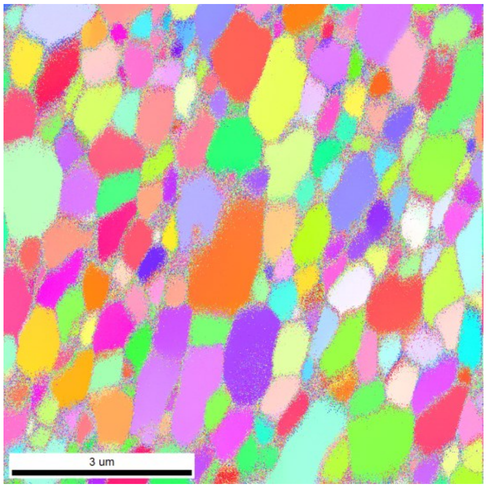

all

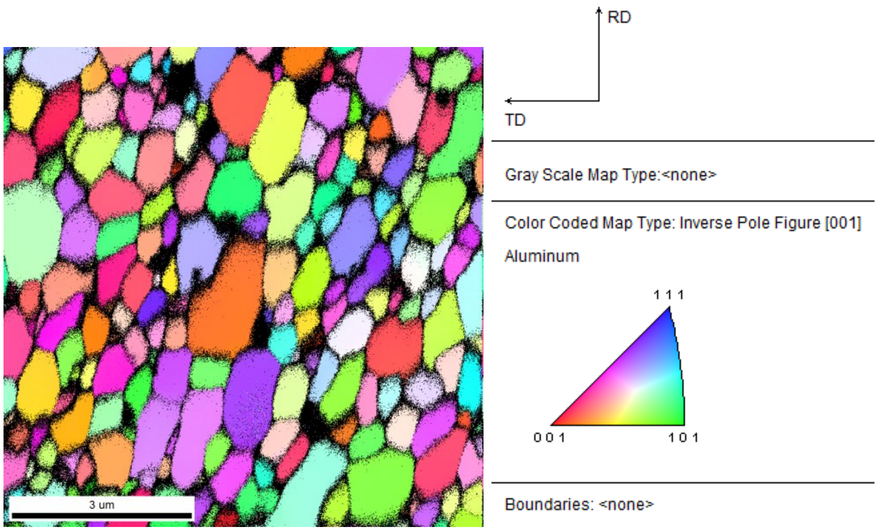

Gray Scale Map Type:<none>

Color Coded Map Type: Inverse Pole Figure [001]

Aluminum

Boundaries: <none>

AL

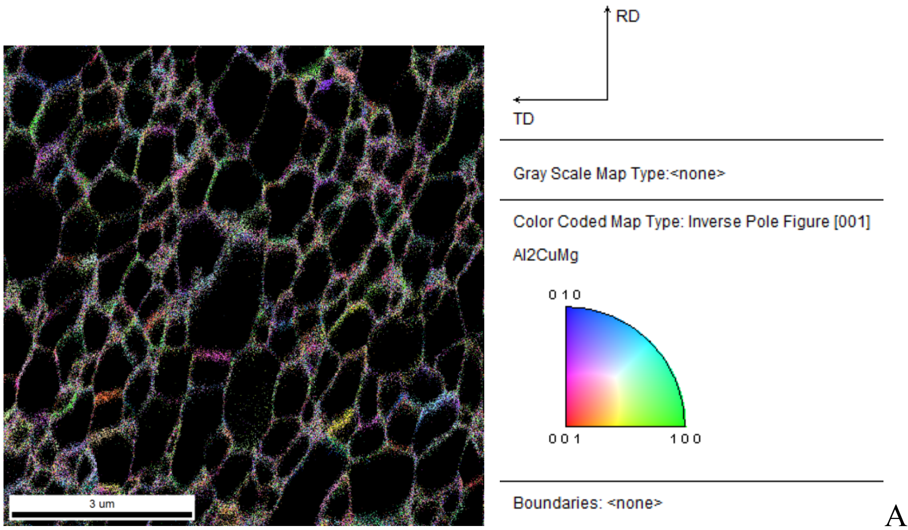

Gray Scale Map Type:<none>

Color Coded Map Type: Inverse Pole Figure [001]

Al2CuMg

Boundaries: <none>

AL2CUMG

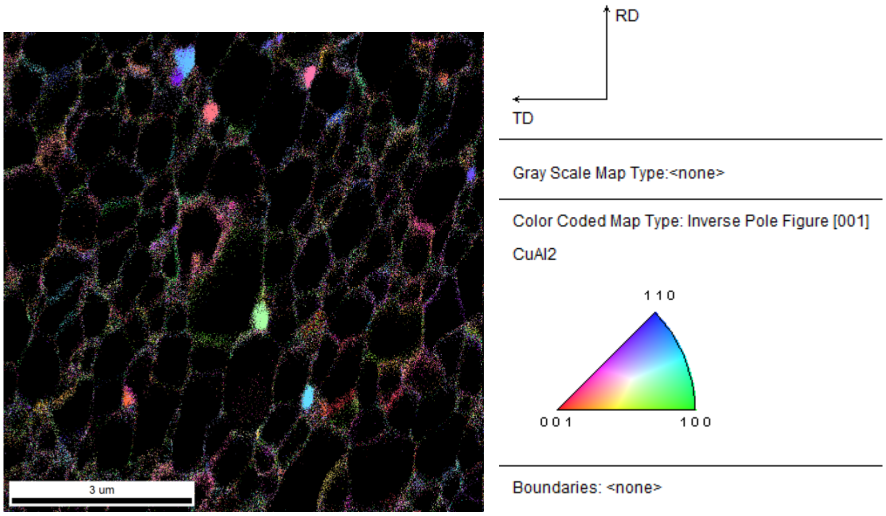

Gray Scale Map Type:<none>

Color Coded Map Type: Inverse Pole Figure [001]

CuAl2

Boundaries: <none>

AL2CU

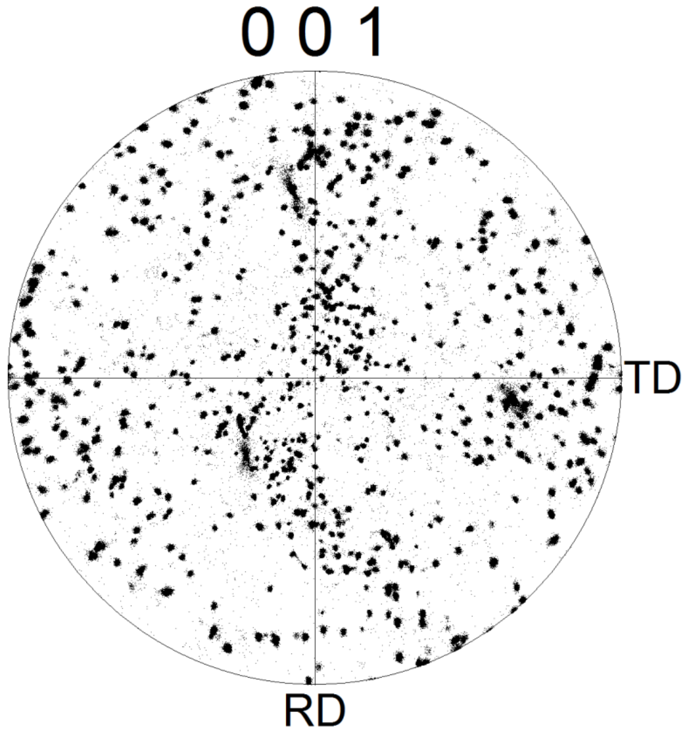

N=8

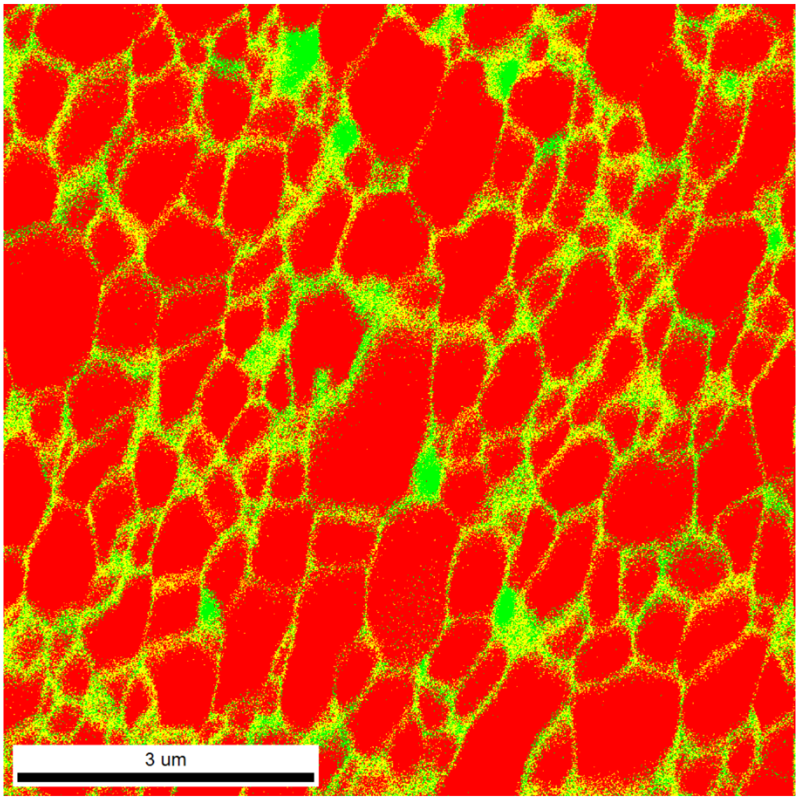

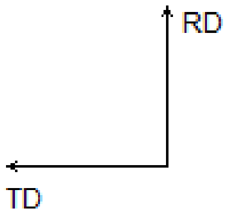

Gray Scale Map Type:<none>

Color Coded Map Type: Phase

	Phase	Total Fraction	Partition Fraction
🟥	Aluminum	0.759	0.759
🟩	CuAl2	0.087	0.087
🟨	Al2CuMg	0.154	0.154

Boundaries: <none>

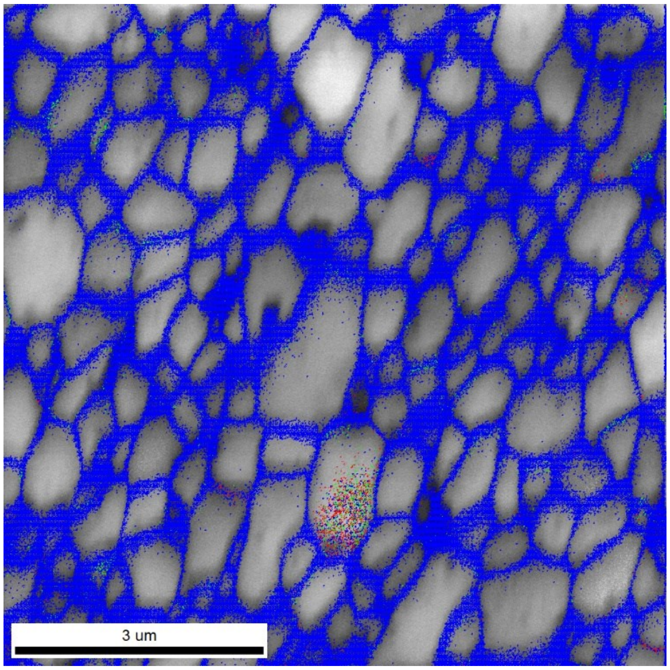

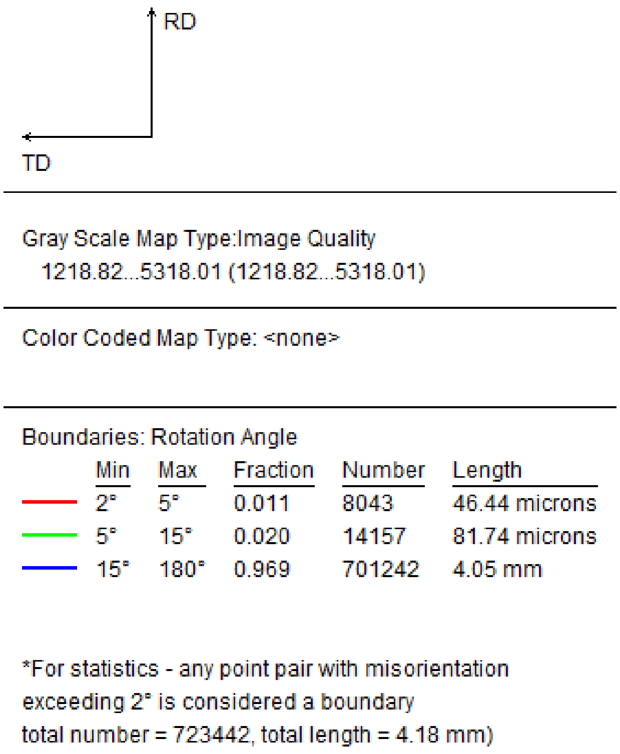

Gray Scale Map Type:Image Quality
1218.82...5318.01 (1218.82...5318.01)

Color Coded Map Type: <none>

Boundaries: Rotation Angle

	Min	Max	Fraction	Number	Length
🟥	2°	5°	0.011	8043	46.44 microns
🟩	5°	15°	0.020	14157	81.74 microns
🟦	15°	180°	0.969	701242	4.05 mm

*For statistics - any point pair with misorientation exceeding 2° is considered a boundary
total number = 723442, total length = 4.18 mm)

TEM

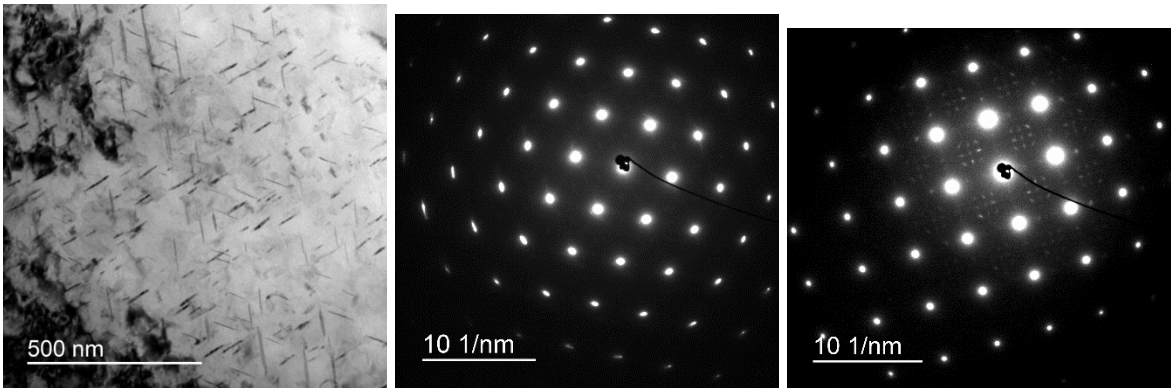

T8

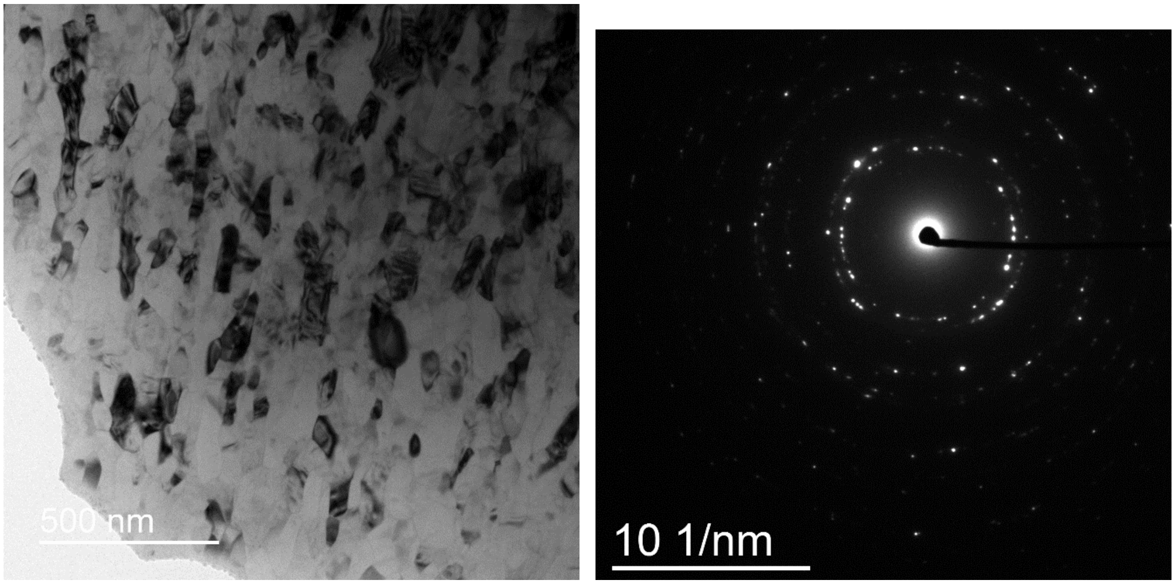

N=1

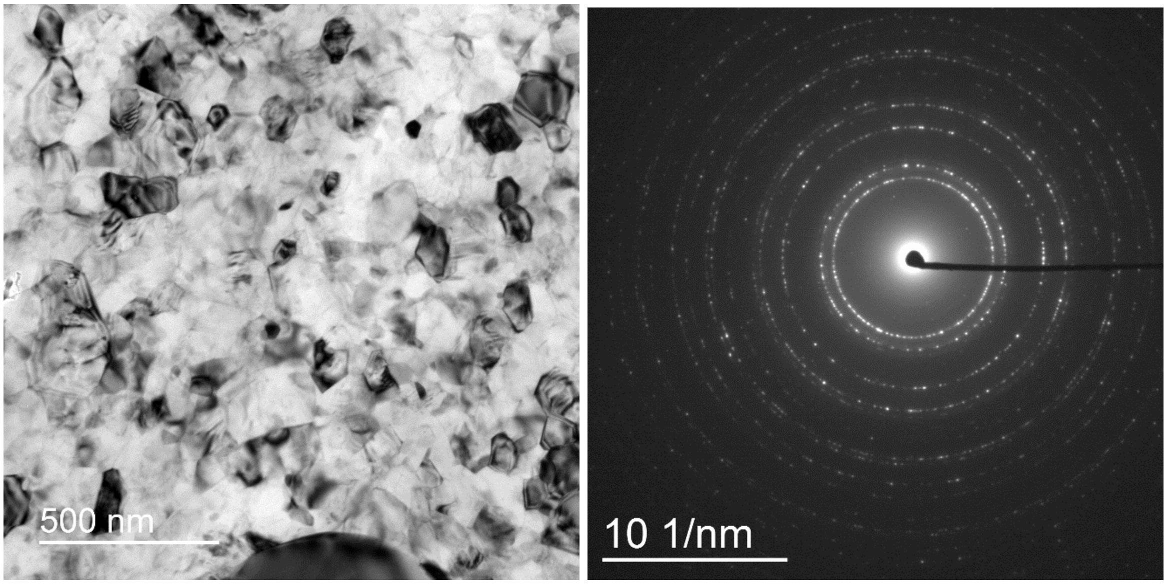

N=2

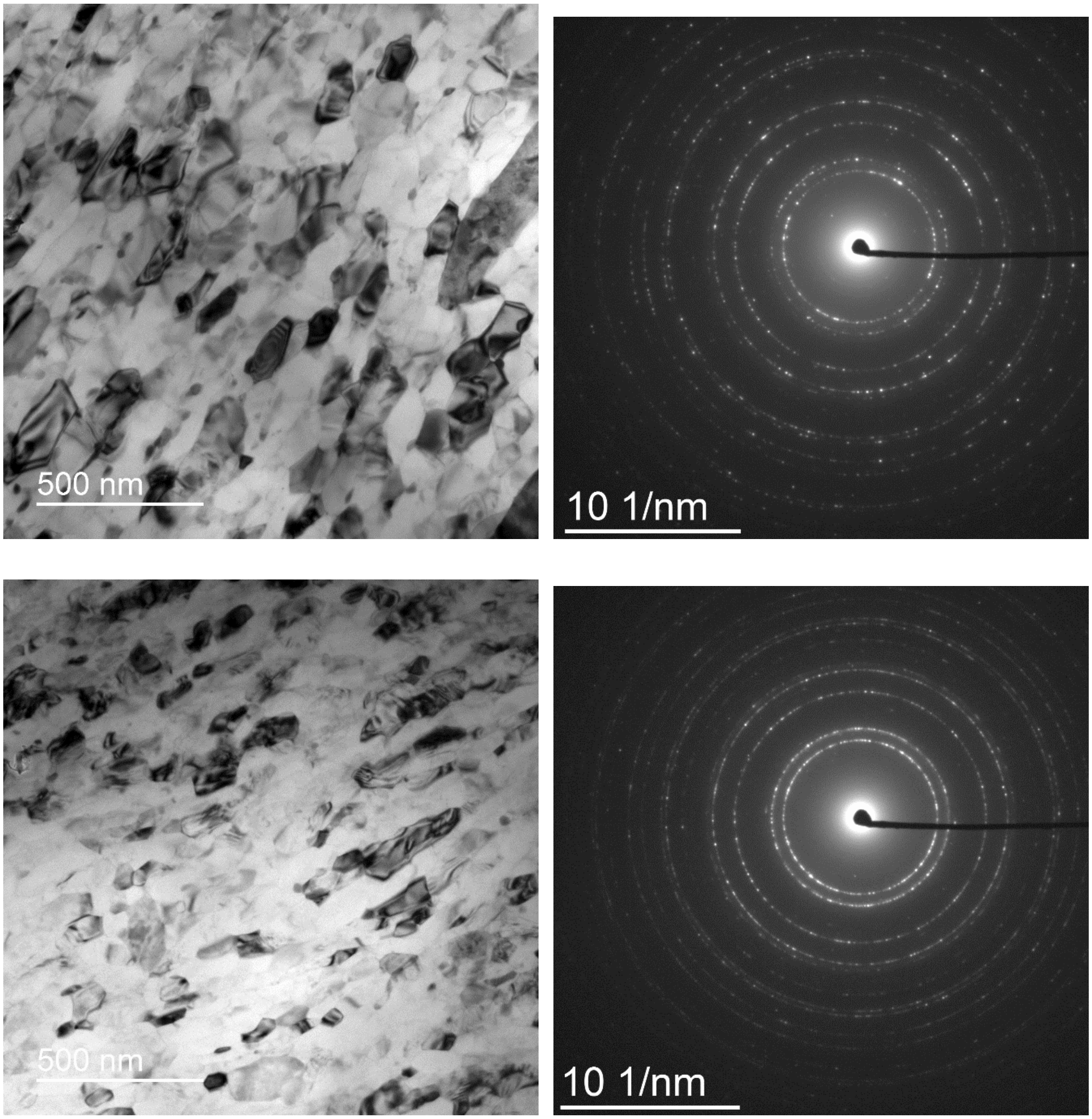

N=4

N=8

TEM bright field images of the T8 sample and the cross-section at half-radius for the HPT samples at N=1, 2, 4, 8. TEM diffraction patterns are subset within each of the bright field images. The T8 diffraction patterns represent the [110] (top) and the [001] (bottom) zone axes

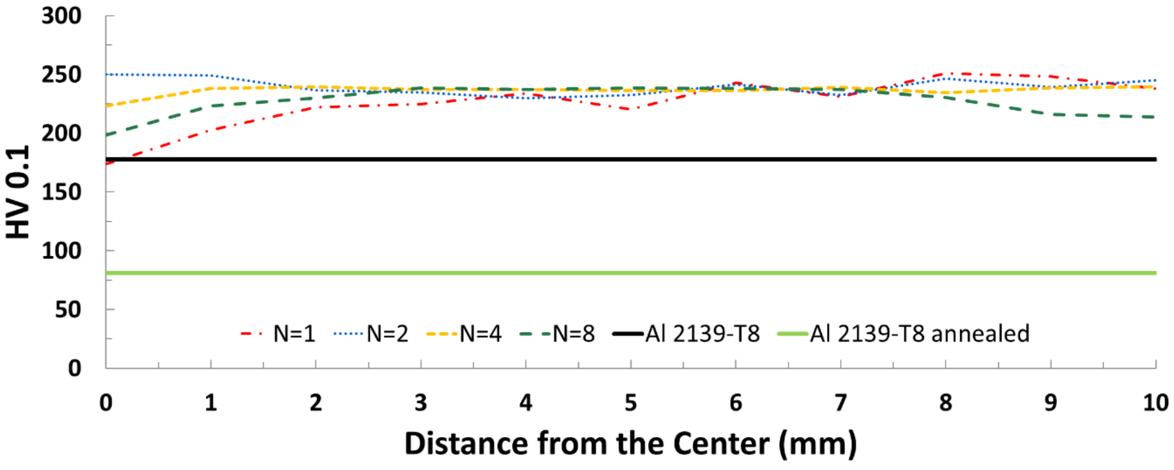

Vickers hardness at 0.1kgf starting from the center of the HPT disc.

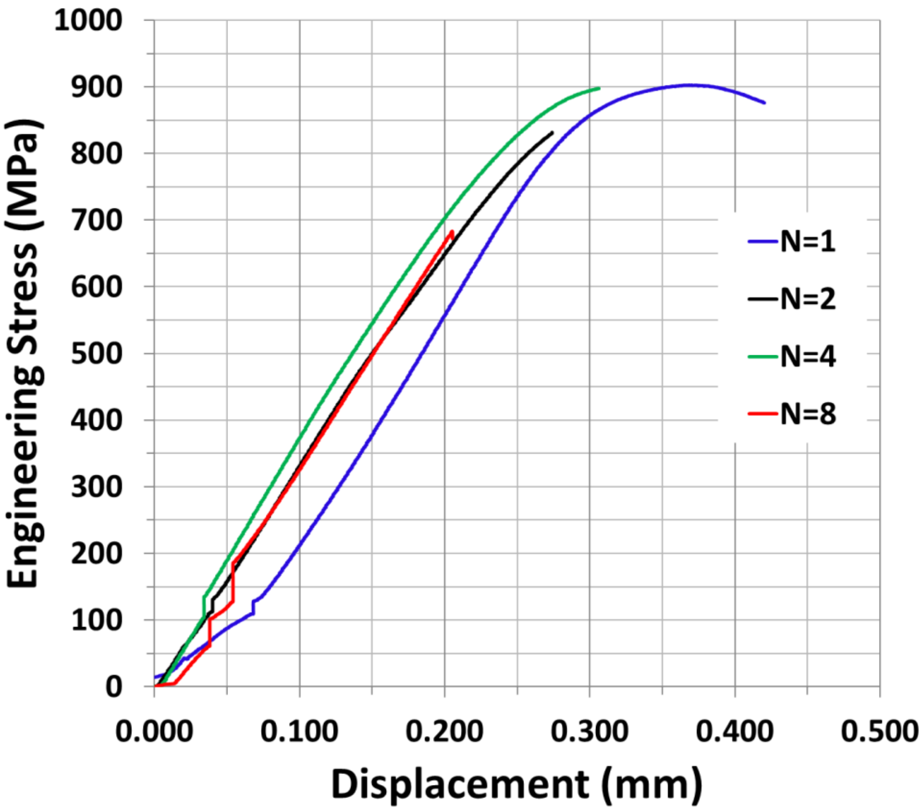

Tensile curves with plateaus removed.

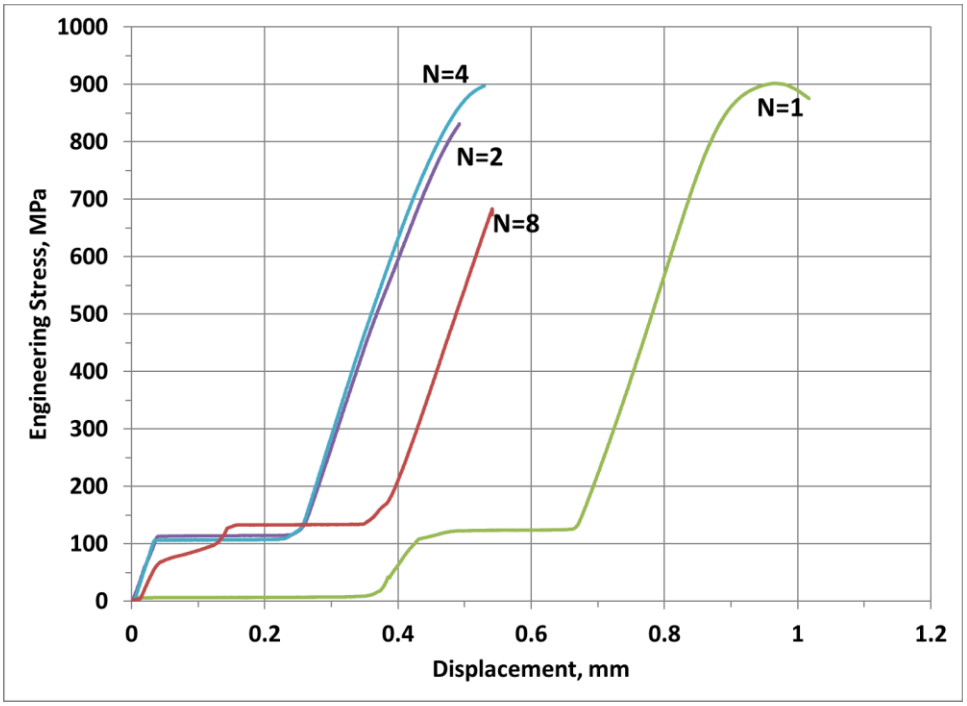

Tensile curves with plateaus

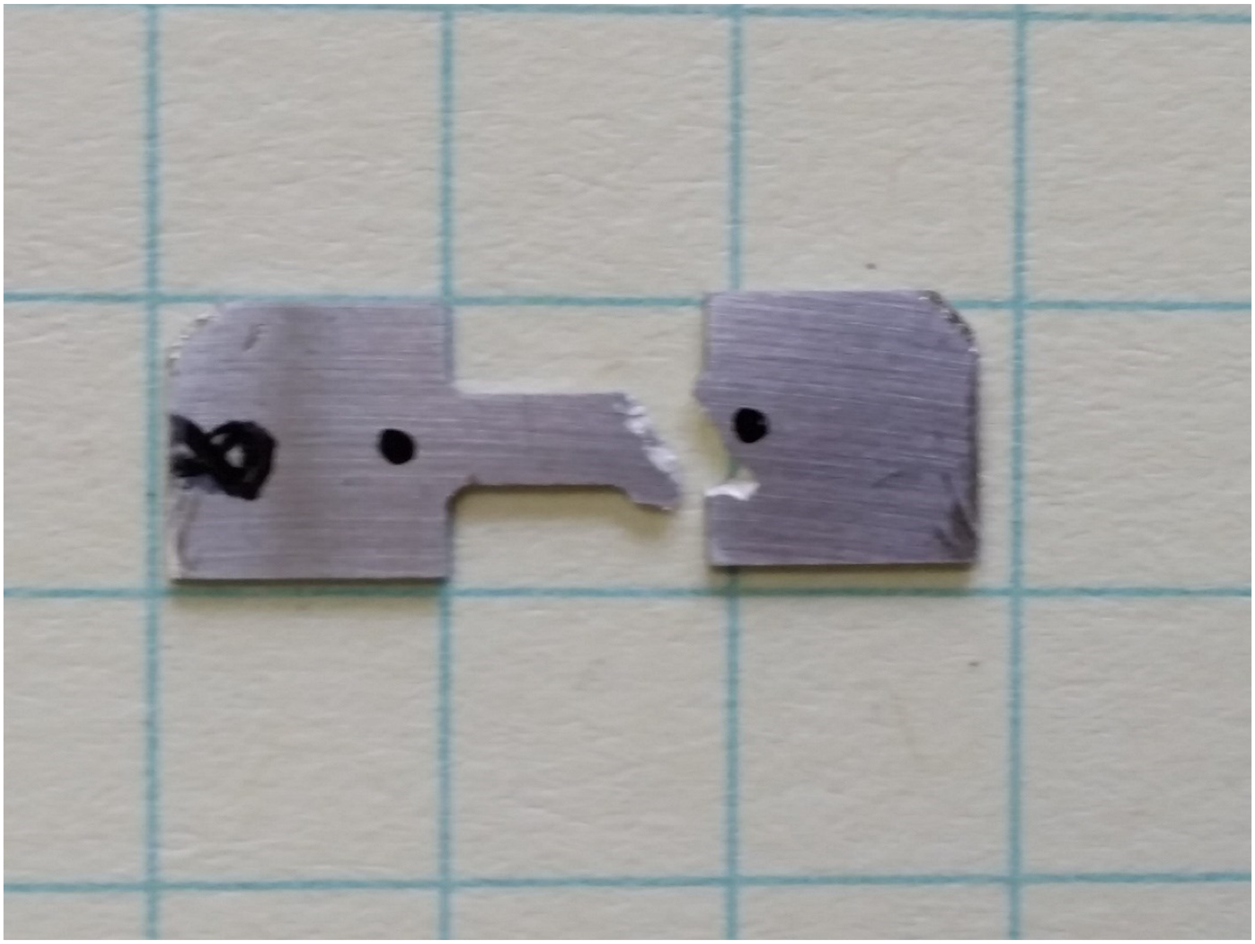

N=8

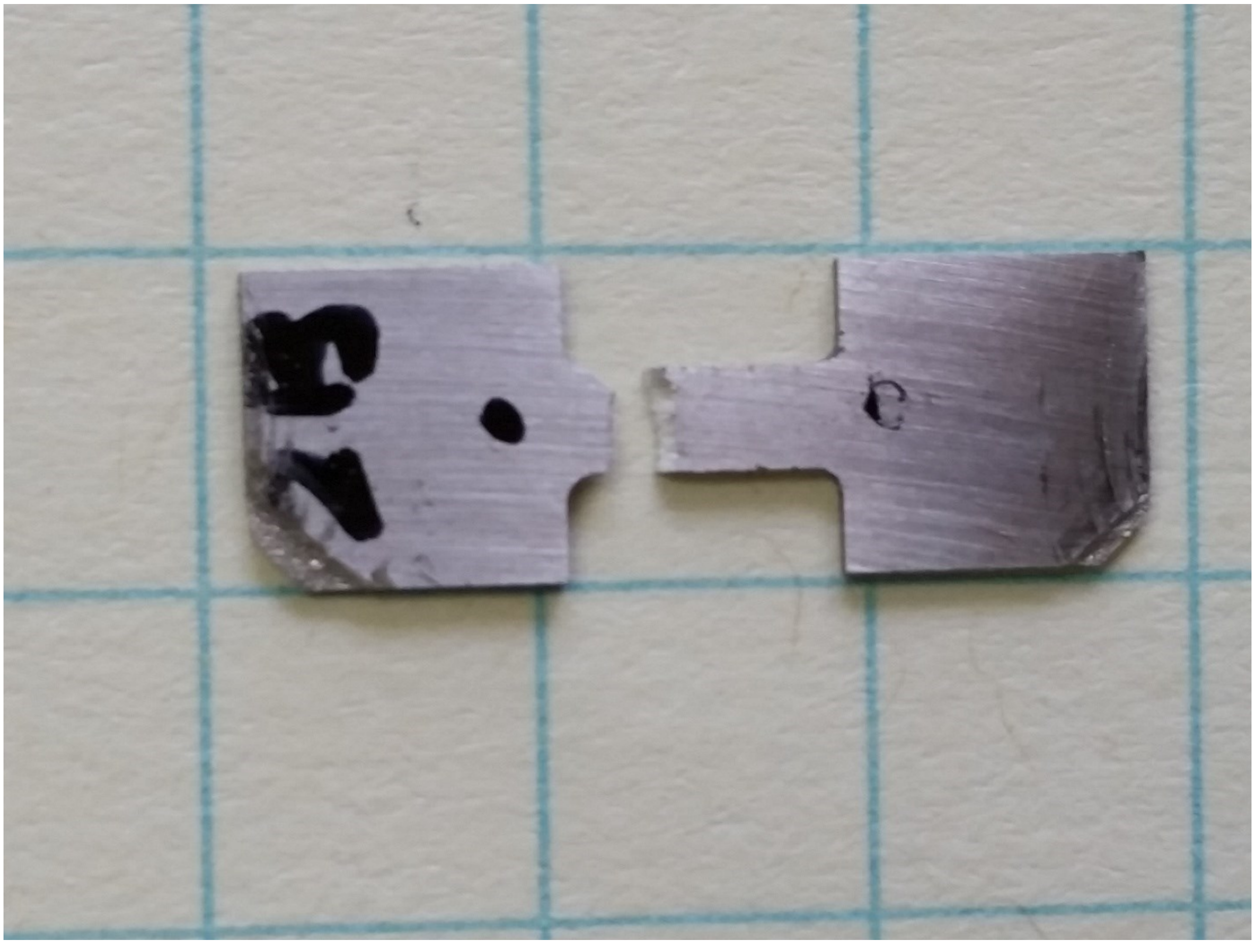

N=2B

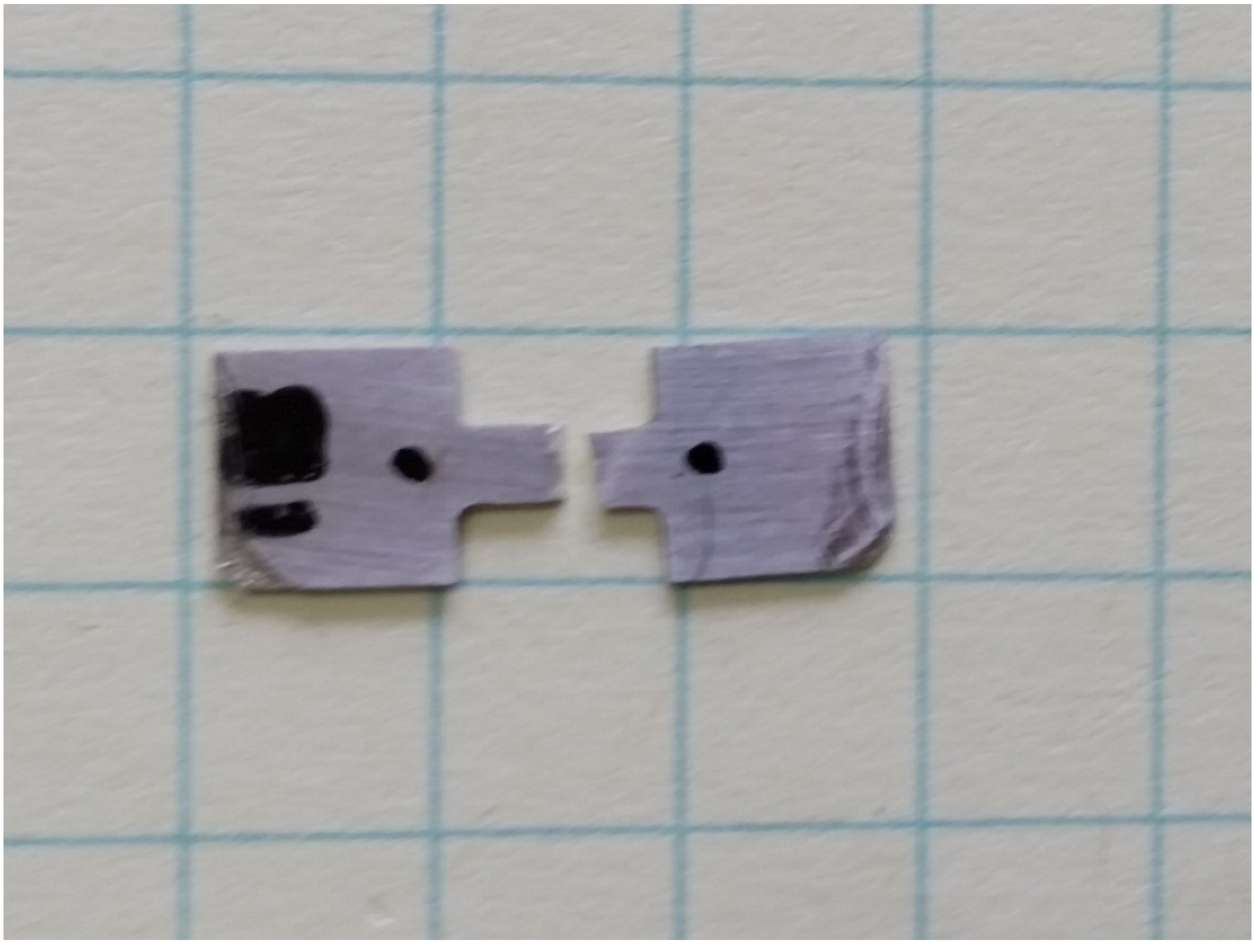

N=1B

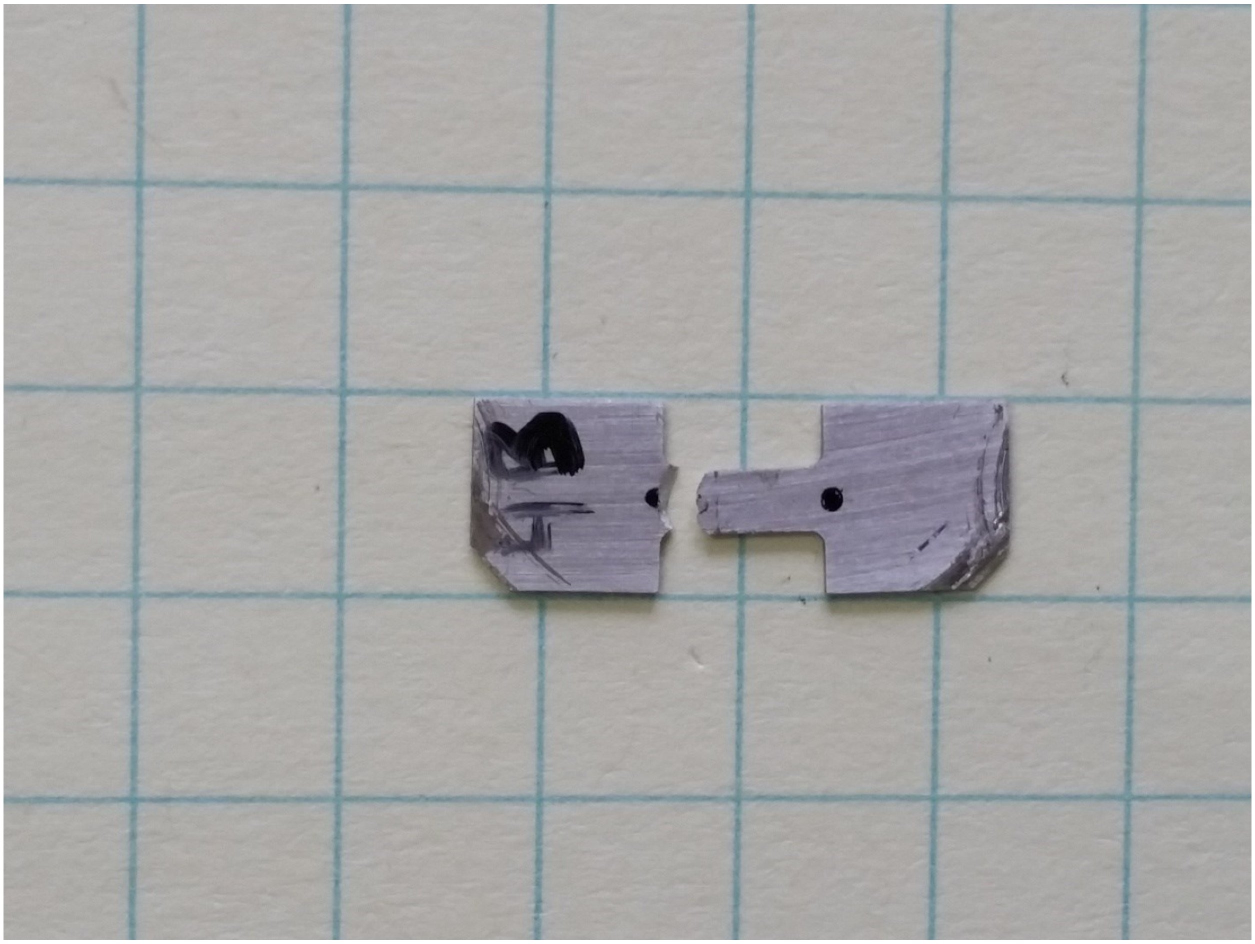

N=4B

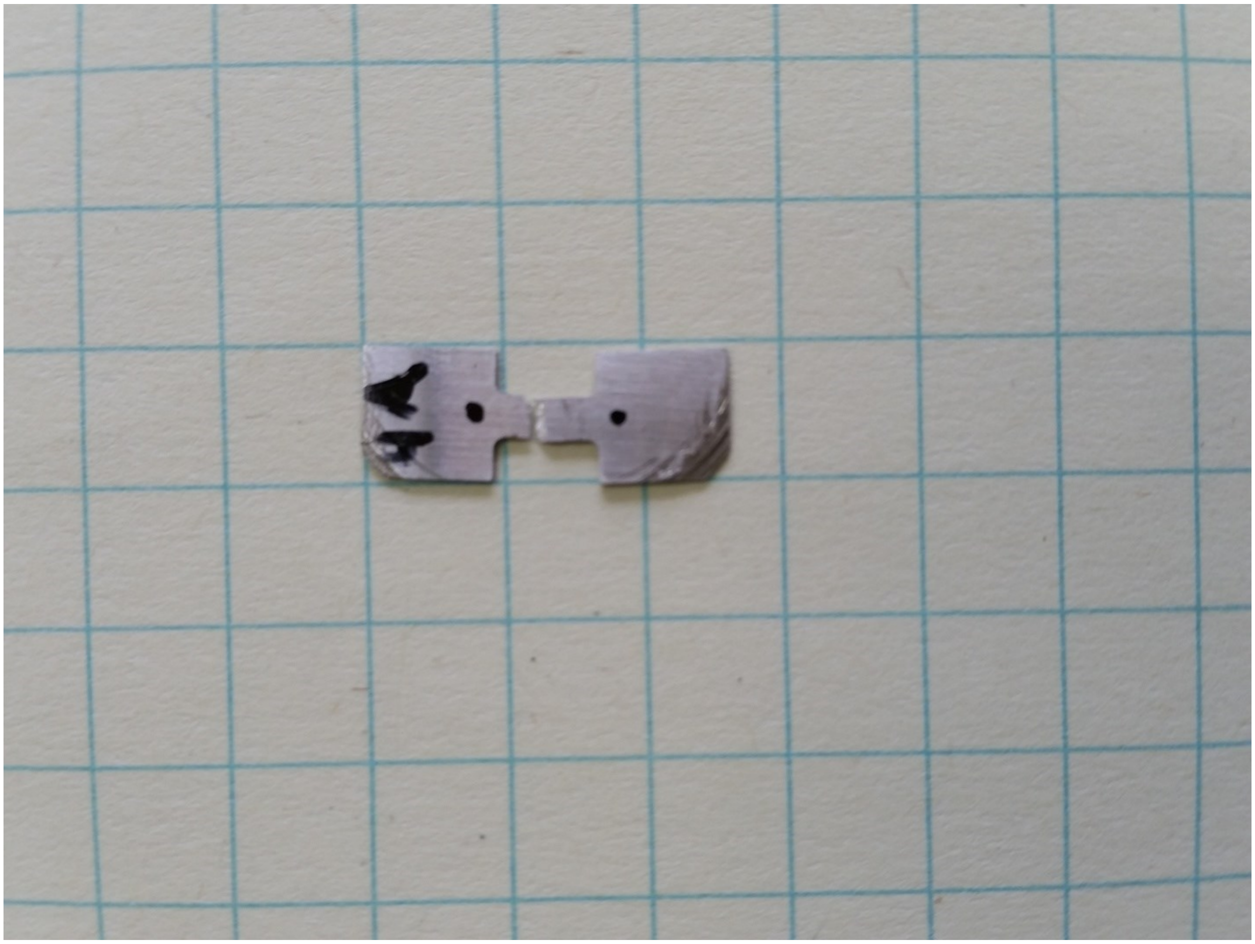

N=4A

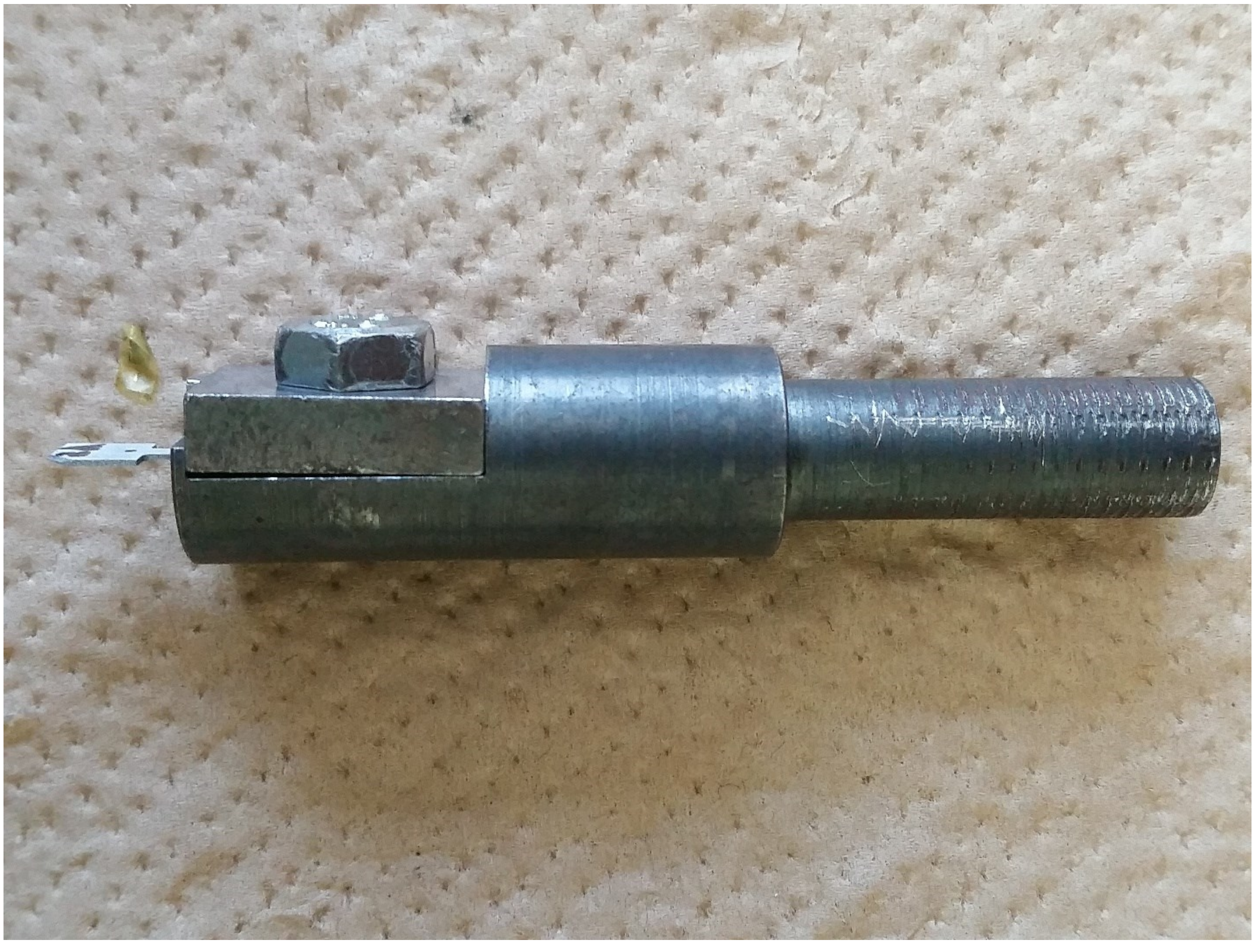

Tensile sample holder with sample in the holder.

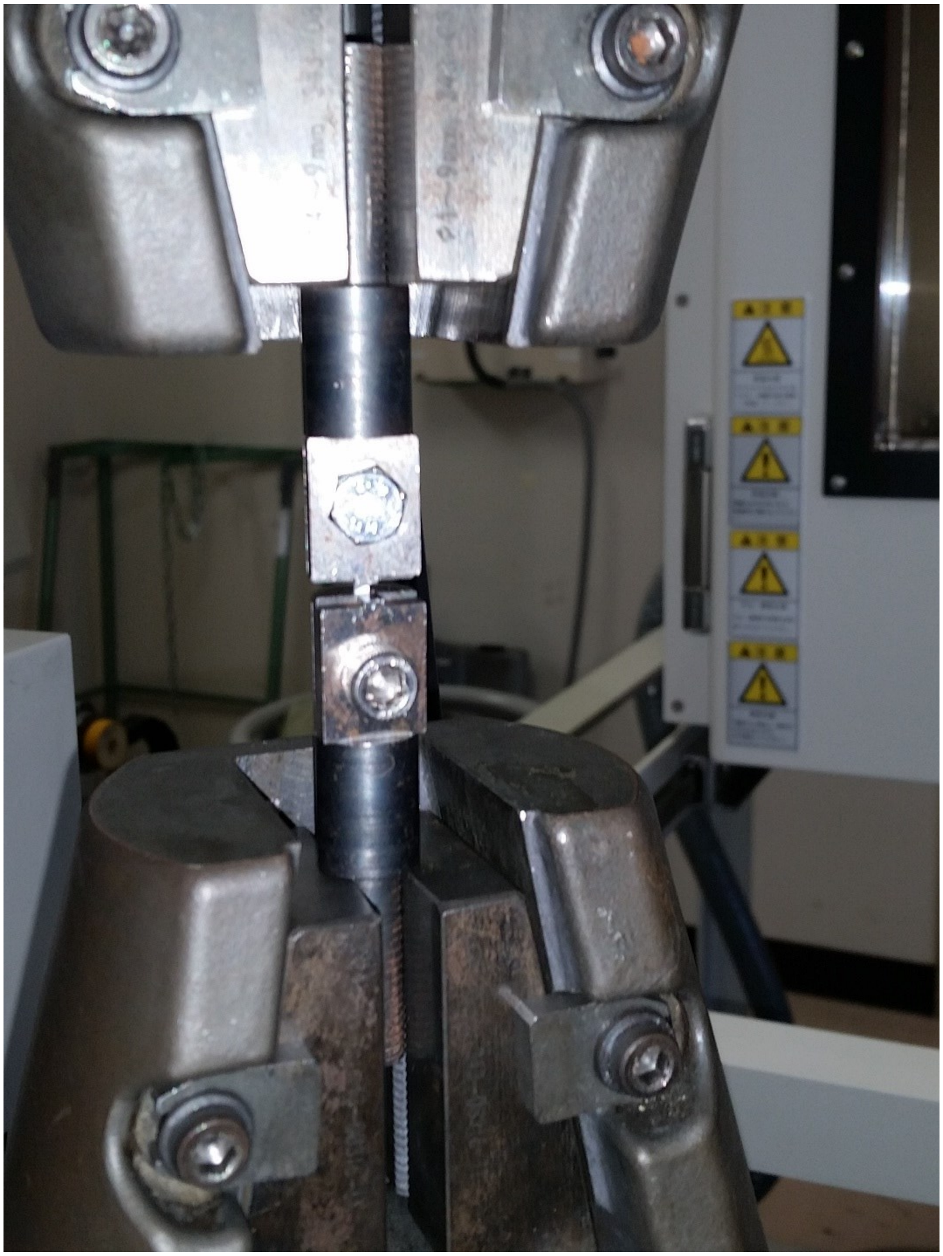

Tensile machine set up with sample